Design and Fabrication of Three-Dimensional Printed Air-Core Transformers for High-Frequency Power Applications

Zikang Tong, *Student Member, IEEE*, Weston D. Braun, *Student Member, IEEE*, and Juan Manuel Rivas-Davila, *Senior Member, IEEE*

***Abstract*—This article presents various designs of toroidal air-core transformers utilizing a 3-D printing and electroplating fabrication methodology. For certain applications and switching frequency regimes, limitations in core-based magnetics force circuit designers to use air-core components, which are conventionally wire-wound, and thus, constrained to simple structures with poor copper coverage. 3-D printing offers a solution to this constraint and provides more flexibility for transformer designs. This article includes design calculations, finite-element method (FEM) simulations, and loss analysis for three different toroidal transformer designs: one which features nested toroids, coupling their N^2 flux, the second which uses stacked toroids, coupling the one-turn flux, and the third which interleaves two windings. Furthermore, the manufacturing procedure presented in this article allows for accurate modeling of the transformer's inductance matrix, which is advantageous over hand-wound air-core components. Additionally, we provide experimental demonstrations, including the implementation of these transformers in 100-W, 30-MHz resonant converters. Lastly, COMSOL FEM design automation MATLAB scripts for the various inductors and transformers discussed in this article are publicly available in the paper by Z. Tong (2019), allowing for fast parametric modeling of magnetic designs.**

***Index Terms*—Finite-element methods (FEM), magnetic analysis, manufacturing automation software, resonant power conversion, transformers.**

I. Introduction

INCREASING power converter switching speeds to high- and very-high-frequencies (3–30 MHz and 30–300 MHz) enables soft-switching resonant converters to achieve higher power densities through the miniaturization of passives [3]–[7]. However, many times in conventional power electronic systems, scaling switching frequency does not simply provide a proportional gain in power density due to limitations of base technologies such as the semiconductors and passives [8]. A large bottleneck being the core-based magnetic components, penalized with second-order effects at high-frequencies, such as core loss, which scales with $kf^{\alpha}V^{\beta}$ [9]–[12], on top of winding loss from skin and proximity effect [13]–[15].

In several applications, circuit designers favor air-core components over traditional core-based magnetics. For example, in magnetic resonance imaging systems, surrounding machinery generates large magnetic fields that can saturate cores inside power supplies, explaining why some converters utilize air-core passives even at lower frequencies (1.7 MHz) [16]. For power conversion applications that scale beyond 30 MHz, [17] claims even when utilizing very low permeability material ($\mu_r = 15$), air-core components exhibit higher quality (Q) factors above 30 MHz. As a result, the optimization of air-core magnetics in high-frequencies remains an attractive area of research.

A large quantity of prior literature has studied and improved designs of core magnetics from 1 to 10 MHz. This includes characterizing and designing structures using low-permeability ferrites, arranging novel winding schemes using Litz wire, and modeling and improving low-cost planar magnetic designs [20]–[30]. However, above 10 MHz, air-core structures become the popular option. Several papers have investigated interesting fabrication techniques, such as printed circuit board (PCB) integration, complex winding patterns using copper foil, and winding geometries to maximize Q factors [19], [31]–[37]. Regardless, the majority of the literature has discussed inductors with little emphasis placed on transformer designs, which are necessary for many topologies and provide galvanic isolation, voltage amplification, and inductive loading. Additionally, many applications benefit greatly from coreless transformers such as lightweight high-voltage power supplies [38] and high-frequency isolated gate drivers [39].

This article extends upon a previously published conference paper [2], which only demonstrates a prototype nested transformer. In this article, we present designs for three different air-core transformers, one featuring a nested setup, where the N^2 fields are linked (H_{N^2} in Fig. 1); another featuring a stacked setup, which couples the one-turn fields ($H_{1\text{-}t}$ in Fig. 1); and a third with interleaved windings. Additionally, this article presents a more thorough characterization of the transformers' losses and presents 30-MHz converters demonstrating the three

Manuscript received August 6, 2019; revised October 19, 2019; accepted December 4, 2019. Date of publication January 5, 2020; date of current version April 22, 2020. This work was supported in part by the Stanford Graduate Fellowship Program, in part by Alcatel-Lucent, and in part by the National Science Foundation Graduate Research Fellowship Program. This paper was presented in part at the *Twentieth IEEE Workshop on Control and Modeling for Power Electronics* in Toronto, ON, Canada, June, 2019 [2]. Recommended for publication by Associate Editor M. Chen. *(Corresponding author: Zikang Tong.)*

The authors are with the Department of Electrical Engineering, Stanford University, Stanford, CA 94305 USA (e-mail: ztong@stanford.edu; wdb@stanford.edu; jmrivas@stanford.edu).

Color versions of one or more of the figures in this article are available online at http://ieeexplore.ieee.org.

Digital Object Identifier 10.1109/TPEL.2020.2963976

TABLE I
LIST OF ADVANTAGES OF 3-D PRINTED AIR-CORE MAGNETIC COMPONENTS OVER TRADITIONAL OPTIONS SUCH AS COMMERCIALLY AVAILABLE COMPONENTS AND WIRE-WOUND PARTS

Commercial structure	Wire-wound/foil-wound structure	3-D Printed structure
✗ Limited availability of geometries, sizes, and inductances ✓ Structurally robust with predictable inductance value ✗ Only available in solenoid shape with unconstrained fields	✓ The designer has the freedom to control size and inductance ✗ Inductance depends on winding configuration and requires iteration ✗ Poor copper coverage with magnetic flux leaking outside of the winding structure between each turn, unless using custom foil or winding design [18], [19]	✓ The designer has the freedom to control size and inductance ✓ Structurally robust with predictable inductance value with a simulation tool ✓ Excellent copper coverage with magnetic flux contained inside of the winding structure, reducing electromagnetic interference and eddy currents

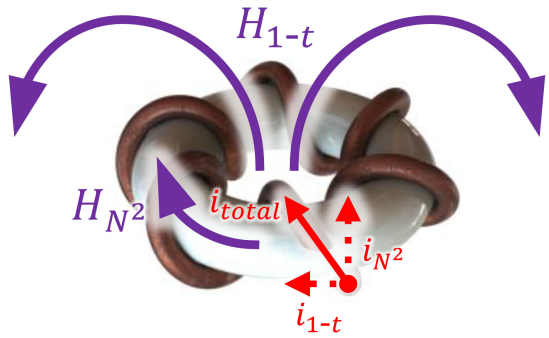

Fig. 1. Example of a toroidal inductor highlighting the radial current i_{N^2}, contributing to the enclosed field H_{N^2}, and the circumferential current i_{1-t}, contributing to H_{1-t}.

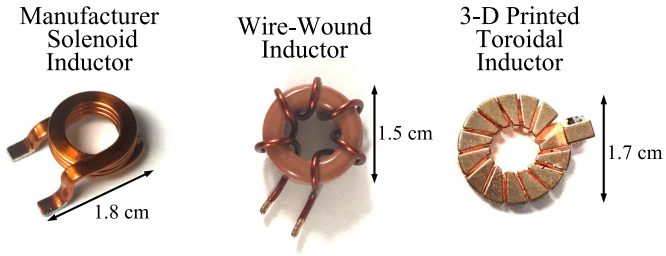

Fig. 2. From left to right: Solenoid air-core inductor manufactured by Coilcraft, wire-wound toroidal inductor with a plastic core, and 3-D printed toroidal inductor.

transformers. We fabricate the windings through 3-D printing a scaffold and electroplating copper onto the surface, similarly experimented by Liang *et al*. for various air-core inductors [40] and [41].

While air-core components are commonly utilized in many high-frequency systems, 3-D printing and rapid prototyping these structures offer many advantages and opportunities compared to conventional methods, which are to wind magnet wire around a nonmagnetic support or use a commercially available winding. Mainly, rapid prototyping offers more design freedom and room for geometric optimization, where papers such as [41] demonstrate a 3-D printed toroidal inductor with optimal cross section leading to higher Q factors. 3-D printed components also provide circuit designers excellent copper coverage. Greater copper coverage, as shown in Fig. 2, allows for more winding surface area, which improves magnetic flux containment within the winding, reduces electromagnetic interference and eddy currents, and lowers parasitic resistances. Compared to current commercially available air-core structures which are mainly solenoids, 3-D printing enables circuit designers to use structurally robust toroids with enclosed magnetic fields. Additionally, it allows the freedom to select the dimensions and geometry, where commercial parts are only available in select geometries, sizes, and inductances. While designers have flexibility in selecting geometry and construction for wire-wound components, it is often difficult to accurately predict and model their inductance matrices and repeatably manufacture identical components. Table I summarizes the benefits of 3-D printed structures in comparison with wire-wound, foil-wound, and commercial parts.

The organization of the article is as follows: Section II presents the fabrication methodology, design analysis, simulation, and experimental results for the nested transformer. Section III presents those for the stacked transformer. Section IV presents the interleaved transformer. Section V explores the losses and ac resistances for the transformers and compares them with a standard foil-wound transformer. Section VI demonstrates all transformer designs in 30-MHz resonant dc–dc converters. Section VII concludes this article. Lastly, the authors provide MATLAB scripts that can automatically generate the toroidal inductor and transformer structures in COMSOL with capabilities to capture inductance and resistance parameters, which are publicly available on Github in [1].

II. ANALYSIS AND DESIGN OF NESTED TOROIDAL TRANSFORMER

The nested toroidal transformer utilizes two toroidal windings with one surrounding the other. In doing so, both toroids couple their N^2 magnetic fields. This transformer structure controls the leakage flux through the number of turns as well as the separation between the two windings. The fabrication scheme is discussed in Section II-A, design procedure in Section II-B, COMSOL simulation in Section II-C, and experimental results in Section II-D for the nested toroidal transformer.

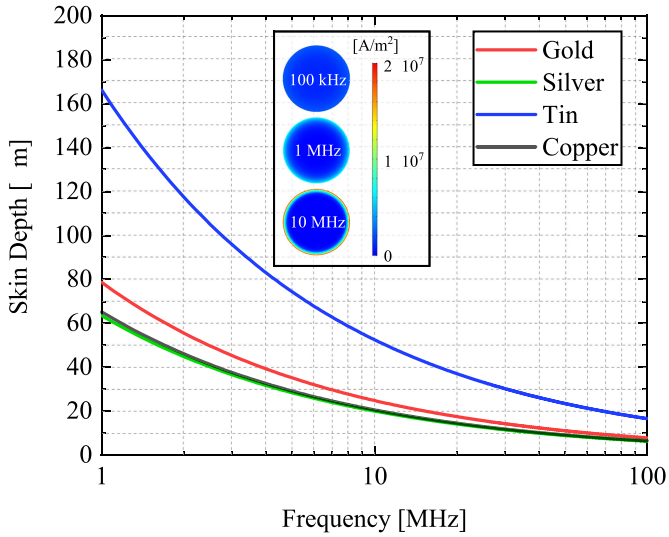

Fig. 3. Solid lines represent the skin depth from 1 to 100 MHz for various metals such as gold, silver, tin, and copper. As frequency increases, the area of the current path shrinks which increases the ac resistance. We also show the cross-sectional current density of a 1 mm diameter wire with 1 A of current at three different frequencies.

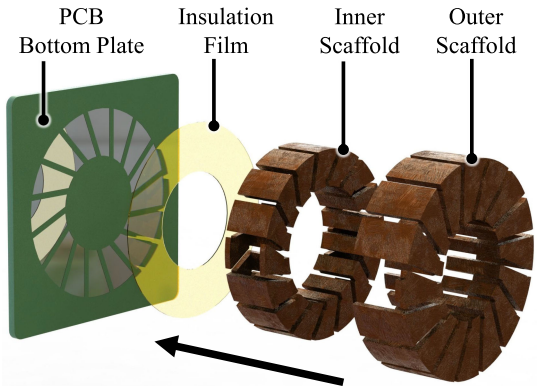

Fig. 4. Fabrication diagram of the toroid-in-toroid transformer structure. The inner winding is one solid piece, while the outer winding is single-turn pieces soldered onto the PCB. The windings are spaced and insulated from one another to maintain galvanic isolation.

A. Fabrication Methodology

The nested toroidal structure contains an inner winding, whose scaffold is 3-D printed using a Formlabs Form 2 stereolithography printer and electroplated to 50–70 μm thickness by Artcraft Plating & Finishing. Since our applications target switching frequencies beyond 10 MHz, our plating thicknesses are beyond two times the skin depth of copper at this frequency. Therefore, it is unnecessary to plate the scaffolds significantly thick. Fig. 3 displays the skin depth versus frequency for various metals. The outer winding is composed of the same plated scaffold except the bottom connections are PCB traces. The outer posts are soldered onto the PCB while covering the inner winding. For ease in prototyping and assembly, Shapeways 3-D Printing Service manufactured the outer scaffold pieces in sterling silver using a sintering process, preventing deformation when soldering. Fig. 4 shows the full manufacturing procedure

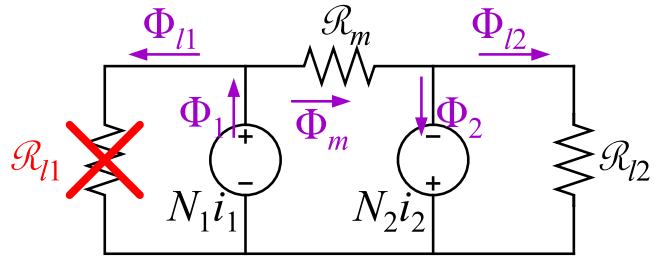

Fig. 5. Magnetic circuit schematic of the transformer. The primary connection is the inner winding ($N_1 i_1$) and the secondary connection is the outer winding ($N_2 i_2$).

for the toroid-in-toroid transformer. Schneider *et al.* [42] utilizes a similar procedure by soldering copper foil cutouts onto a PCB to form toroidal inductors. An insulating film, such as Kapton, can be used to surround the inner winding to prevent shorting to the outer winding. This is not always necessary depending on the voltage isolation requirement.

B. Design Procedure

To size the winding dimensions and number of turns, it is necessary to formulate the transformer's inductance matrix, since this defines the 2-port current–voltage relationship. To obtain the inductance matrix, we begin by developing the magnetic circuit model shown in Fig. 5, and to provide design simplicity, we acknowledge the following assumptions.

1) Neglect sharp corner effects of the H-field, so that Ampere's law can simply determine the H-field inside the square cross section of the toroid.
2) Neglect the leakage flux of the inner winding because the flux inside the inner cross section is enclosed by the outer cross section. In Fig. 5, $\mathcal{R}_{l1}$, crossed out by the red X, approaches infinite.

Based on these preconditions, we first calculate the reluctances, as shown in Fig. 5. $\mathcal{R}_m$ is the mutual reluctance, or the flux path shared by both the inner and outer winding, while $\mathcal{R}_{l2}$ is the leakage reluctance, in other words, the flux path inside the outer winding but outside of the inner winding, as shown in Fig. 6.

To calculate the reluctances, Ampere's law in (1) obtains the expression for the H-field inside the toroid ($H = \frac{Ni}{2\pi r}$) exemplified in Fig. 7, where N is the number of turns of the toroid and i is the current

$$\oint_c B \cdot dl = \mu_0 I_{\text{enc}}. \tag{1}$$

Then, the surface integral of the H-field inside of the inner cross section gives the mutual flux Φ_m and the surface integral of the area between the inner and outer cross section provides the leakage flux Φ_{l2}. Using (2) and (3), the reluctances equates to Ni over the calculated Φ's

$$\mathcal{R}_m = \frac{Ni}{\Phi_m} = \frac{Ni}{\iint_S \mu_0 H dS} = \frac{Ni}{\mu_0 h_{\text{prim}} \int_{r_{i,\text{prim}}}^{r_{o,\text{prim}}} \frac{Ni}{2\pi r} dr}$$

$$= \frac{2\pi}{\mu_0 h_{\text{prim}} \ln\left(\frac{r_{o,\text{prim}}}{r_{i,\text{prim}}}\right)} \tag{2}$$

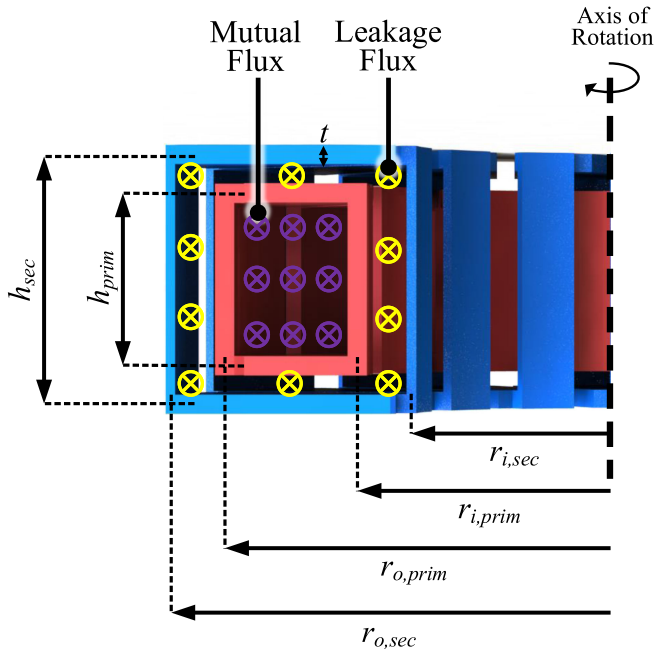

Fig. 6. Cross-sectional cutout of the toroidal transformer, highlighting the mutual flux Φ_m and leakage flux Φ_{l2}. The red inner winding is the primary winding and the blue outer winding is the secondary.

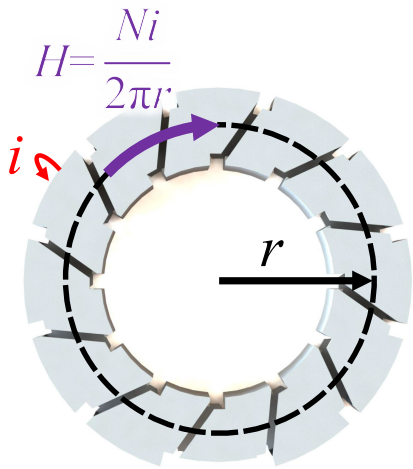

Fig. 7. Top view of the toroid, where the H-field can be calculated with Ampere's law.

$$\begin{aligned}\mathcal{R}_{l2} &= \frac{Ni}{\Phi_2 - \Phi_m} \\ &= \frac{Ni}{\mu_0 h_{sec}\int_{r_{i,\text{sec}}}^{r_{o,\text{sec}}} \frac{Ni}{2\pi r}dr - \mu_0 h_{\text{prim}}\int_{r_{i,\text{prim}}}^{r_{o,\text{prim}}} \frac{Ni}{2\pi r}dr} \\ &= \frac{2\pi}{\mu_0\left[h_{sec}\ln\left(\frac{r_{o,\text{sec}}}{r_{i,\text{sec}}}\right) - h_{\text{prim}}\ln\left(\frac{r_{o,\text{prim}}}{r_{i,\text{prim}}}\right)\right]}. \end{aligned} \tag{3}$$

Second once the reluctance values are known, the magnetic circuit determines the relationship between the flux linkage λ, defined as $N\Phi$, and the currents, resulting in the inductance matrix in

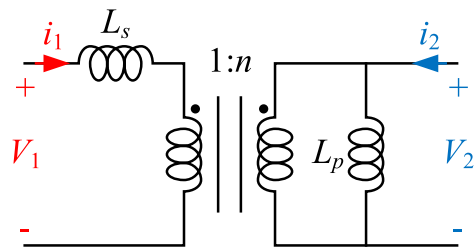

Fig. 8. Schematic of the cantilever transformer model.

TABLE II
LIST OF PARAMETERS FOR THE EXAMPLE NESTED TRANSFORMER

	Outer winding	Inner winding
Outer diameter [mm]	38	32.6
Inner diameter [mm]	16	24
Height [mm]	12.5	6.5
Thickness [mm]	1.5	1.5
Separation distance [mm]	1.5	1.5
Number of turns per winding	14	20

$$\begin{aligned}\begin{bmatrix}\lambda_1\\ \lambda_2\end{bmatrix} \equiv \begin{bmatrix}N_1\Phi_1\\ N_2\Phi_2\end{bmatrix} &= \begin{bmatrix}L_{11} & L_{12}\\ L_{21} & L_{22}\end{bmatrix}\begin{bmatrix}i_1\\ i_2\end{bmatrix} \\ &= \begin{bmatrix}\frac{N_1^2}{\mathcal{R}_m} & \frac{N_1N_2}{\mathcal{R}_m}\\ \frac{N_1N_2}{\mathcal{R}_m} & \frac{N_2^2}{\mathcal{R}_m} + \frac{N_2^2}{\mathcal{R}_{l2}}\end{bmatrix}\begin{bmatrix}i_1\\ i_2\end{bmatrix} \\ &= \begin{bmatrix}L_s + \frac{L_p}{n^2} & \frac{L_p}{n}\\ \frac{L_p}{n} & L_p\end{bmatrix}\begin{bmatrix}i_1\\ i_2\end{bmatrix} z. \end{aligned} \tag{4}$$

The inductance matrix provides the transformation between various transformer models, and (4) expresses the matrix using cantilever parameters (L_s, L_p, and n). For this article, the cantilever model we will be using features the series inductance at the primary and the shunt inductance at the secondary, as shown in Fig. 8. Lastly, differentiating (4) results in the voltage–current equation for the transformer expressed in

$$\frac{d}{dt}\begin{bmatrix}N_1\Phi_1\\ N_2\Phi_2\end{bmatrix} = \begin{bmatrix}V_1\\ V_2\end{bmatrix} = \begin{bmatrix}L_{11} & L_{12}\\ L_{21} & L_{22}\end{bmatrix}\frac{d}{dt}\begin{bmatrix}i_1\\ i_2\end{bmatrix}. \tag{5}$$

1) Design Example: As an example, we calculate the inductance matrix of a transformer with physical parameters listed in Table II. The first step is to solve for the mutual reluctance $\mathcal{R}_m$ following (2). Note that because the structural thickness consumes part of the cross-sectional area, the height and outer diameter are reduced by 1.5 mm and the inner diameter increases by 1.5 mm. Equation (6) provides the values used to calculate $\mathcal{R}_m$ in this example, and the final value is 5.04×10^9 H^{-1}

To calculate $\mathcal{R}_m$

$$h_{\text{prim}} = 6.5 - 1.5 = 5\,\text{mm}$$

$$r_{o,\text{prim}} = \frac{32.6 - 1.5}{2} = 15.55\,\text{mm}$$
$$r_{i,\text{prim}} = \frac{24 + 1.5}{2} = 12.75\,\text{mm}. \quad (6)$$

Next, we utilize (3) to calculate the secondary leakage reluctance $\mathcal{R}_{l2}$. Similarly, we adjust the height and radius values by the toroid thickness, as shown in (7). Note that when calculating $\mathcal{R}_{l2}$, the values h_{prim} and $2r_{o,\text{prim}}$ must add the wall thickness while $2r_{i,\text{prim}}$ subtracts the wall thickness, which is different than the $\mathcal{R}_m$ case because the thickness of the cross section of the primary toroid consumes the flux path of the secondary toroid. The resulting $\mathcal{R}_{l2}$ is $1.05 \times 10^9\ \text{H}^{-1}$. Lastly, using these reluctance values, N_1, and N_2, we obtain the inductance matrix through (8).

$$\begin{aligned}
&\text{To calculate } \mathcal{R}_{l2}\\
h_{\text{prim}} &= 6.5 + 1.5 = 8\,\text{mm}\\
r_{o,\text{prim}} &= \frac{32.6 + 1.5}{2} = 17.05\,\text{mm}\\
r_{i,\text{prim}} &= \frac{24 - 1.5}{2} = 11.25\,\text{mm}\\
h_{\text{sec}} &= 12.5 - 1.5 = 11\,\text{mm}\\
r_{o,\text{sec}} &= \frac{38 - 1.5}{2} = 18.25\,\text{mm}\\
r_{i,\text{sec}} &= \frac{16 + 1.5}{2} = 8.75\,\text{mm} \quad (7)
\end{aligned}$$

$$\begin{bmatrix} L_{11} & L_{12} \\ L_{21} & L_{22} \end{bmatrix} = \begin{bmatrix} \frac{N_1^2}{\mathcal{R}_m} & \frac{N_1 N_2}{\mathcal{R}_m} \\ \frac{N_1 N_2}{\mathcal{R}_m} & \frac{N_2^2}{\mathcal{R}_m} + \frac{N_2^2}{\mathcal{R}_{l2}} \end{bmatrix} = \begin{bmatrix} 79\,\text{nH} & 56\,\text{nH} \\ 56\,\text{nH} & 226\,\text{nH} \end{bmatrix}. \quad (8)$$

The calculated values neglect the inductance and coupling produced by the one-turn magnetic fields of the toroids. Therefore, to further improve the accuracy of the inductance matrix, L_{11} and L_{22} can be increased by, respectively, the primary and secondary toroid's one-turn inductance, as obtained from [43], and formulated as

$$L_{1-t} = \frac{d_o + d_i}{4}\mu_0 \left[\ln\left(8\frac{d_o + d_i}{d_o - d_i}\right) - 2\right]. \quad (9)$$

The one-turn inductance of the primary equates to 35 and 17 nH for the secondary. Thus, the final values for L_{11} and L_{22} are 114 and 243 nH. Table V in Section II-B compares the calculated inductance matrix with simulated and experimental results.

C. Simulation Results

To validate the design, we simulated the example structure in COMSOL Multiphysics 5.2a using the magnetic fields physics module. The transformer is modeled as a 2-port network driven by two lumped ports, resembling current sources. In Fig. 9, lumped port 1 drives the primary (inner) winding and lumped port 2 drives the secondary (outer) winding. To obtain the inductance matrix, we run two frequency domain simulations: first set $i_1 = 1$ A, $i_2 = 0$ A, and second set $i_1 = 1$ A, $i_2 = 1$ A.

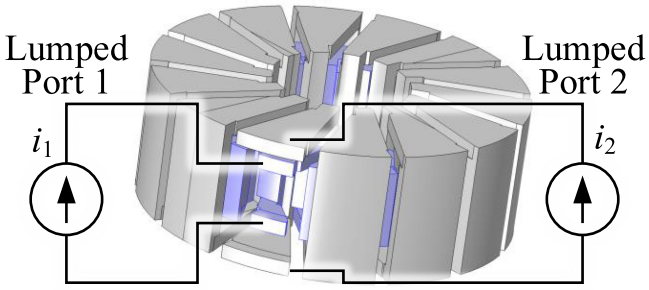

Fig. 9. Schematic of COMSOL simulation procedure. Two lumped ports, resembled as current sources with controllable amplitudes and frequencies, are set at the two ports of the transformer. The inner winding is highlighted in blue.

TABLE III
LIST OF IMPEDANCES AT 20 MHZ DERIVED FROM COMSOL SIMULATION OF THE EXAMPLE NESTED TRANSFORMER AS WELL AS CALCULATED INDUCTANCE MATRIX PARAMETERS FROM THE IMPEDANCES

Parameter	Value
$\hat{V_1}/\hat{i_1}$ [Ω], 1 A in primary	$0.113 + 14.226j$
$\hat{V_1}/\hat{i_1}$ [Ω], 1 A in primary and secondary	$0.185 + 24.235j$
$\hat{V_2}/\hat{i_2}$ [Ω], 1 A in primary and secondary	$0.368 + 43.552j$
L_{11} [nH]	113
L_{12}, L_{21} [nH]	80
L_{22} [nH]	267

For frequency domain simulations, the simulation requires a frequency of interest or a range of frequencies. We perform all simulations at 20 MHz.

COMSOL provides the voltage phasors at the two ports, from which we obtain the equivalent inductance at each port through

$$L_{\text{port1}} = \text{Im}\left\{\frac{\hat{V_1}}{2\pi f \hat{i_1}}\right\},\ L_{\text{port2}} = \text{Im}\left\{\frac{\hat{V_2}}{2\pi f \hat{i_2}}\right\}. \quad (10)$$

The first simulation, where $i_1 = 1$ A and $i_2 = 0$ A, gives L_{11}, which is the inductance at port 1, since $V_1 = j\omega L_{11} i_1$. In the second simulation where $i_1 = 1$ A and $i_2 = 1$ A, $V_1 = j\omega(L_{11} + L_{12})i_1$, therefore the inductance at port 1 is $L_{11} + L_{12}$, from which we can obtain L_{12} and L_{21}, since $L_{12} = L_{21}$. Likewise, the inductance at port 2 is equivalent to $L_{21} + L_{22}$, from which we obtain L_{22}. Table III lists the values obtained from the simulation as well as the inductance matrix converted from the simulation values. Also, Fig. 10 shows the magnetic field intensity distribution inside the cross sections in both simulations. As shown in Fig. 10(a), when only the primary is excited, the field intensity is only concentrated inside the inner winding's cross section. In Fig. 10(b), when both the primary and secondary are excited, the field is much more intense inside the inner cross section because both windings contribute flux in that region. Outside of the primary cross section, the field is less intense because only the secondary winding contributes flux.

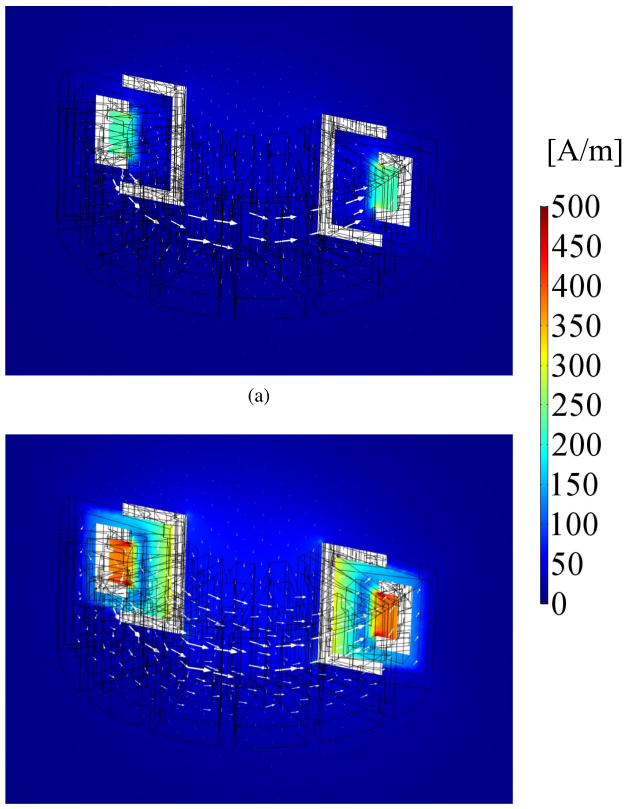

Fig. 10. (a) Magnetic field intensity (H-field) colormap of the nested transformer's center cross section with a 20-MHz current signal of an amplitude of 1 A injected into the primary winding. The white arrows represent the direction of the H-field. (b) H-field colormap of the nested transformer with a 1 A, 20 MHz current injected into both primary and secondary windings.

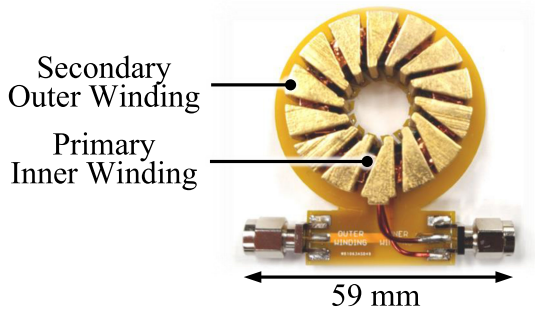

Fig. 11. Nested transformer fabricated using the procedure from Section II-A and dimensions listed in Table II in Section II-B.

D. Experimental Results

Based on the design example in Section II-B, we construct the nested toroidal transformer shown in Fig. 11 with physical dimensions and the number of turns listed in Table II. To obtain the transformer's inductance matrix, we used a Keysight E5061B impedance analyzer and calibrated using open, short, and 50-Ω load with the Keysight 16195B calibration kit. We measured three inductance values using the one-port reflection method on the impedance analyzer as follows:

1) the equivalent inductance at the primary with the secondary open $L_{1,\text{open}}$;
2) the inductance at the secondary with the primary open $L_{2,\text{open}}$;
3) the inductance at the secondary with the primary shorted $L_{2,\text{short}}$.

From these three measurements, we can then derive the inductance matrix based on (11), where k is the coupling coefficient

$$L_{11} = L_{1,\text{open}}$$
$$L_{12}, L_{21} = k\sqrt{L_{1,\text{open}} L_{2,\text{open}}},\ k = \sqrt{1 - \frac{L_{2,\text{short}}}{L_{2,\text{open}}}}$$
$$L_{22} = L_{2,\text{open}}. \tag{11}$$

The measured values and converted inductance matrix parameters for the demonstrated transformer are listed in Table IV.

Lastly, Table V compares the experimental inductance matrix values with COMSOL simulations and first-order hand calculations. While the calculated values for L_{11} and L_{22} match the simulation and experimental results well, the calculated mutual inductance L_{12} and L_{21} is slightly lower than the simulated and experimental values because we choose to neglect the coupling of the one-turn fields. Although the one-turn coupling can be accounted for, we choose to ignore this since the mathematical analysis involves computationally complex elliptic integrals, as discussed in [44].

TABLE IV
MEASURED VALUES OF THE NESTED TRANSFORMER SHOWN IN Fig. 11. SECOND HALF OF THE TABLE LISTS THE INDUCTANCE MATRIX PARAMETERS DERIVED FROM THE MEASURED VALUES

Parameter	Value
$L_{1,\text{open}}$ [nH]	125
$L_{2,\text{open}}$ [nH]	264
$L_{2,\text{short}}$ [nH]	226
L_{11} [nH]	125
L_{12}, L_{21} [nH]	69
L_{22} [nH]	264

TABLE V
COMPARISON OF INDUCTANCE MATRIX VALUES AND CANTILEVER PARAMETERS (L_s, L_p, n) BETWEEN FIRST-ORDER CALCULATIONS, COMSOL SIMULATION, AND EXPERIMENTALLY BUILT NESTED TRANSFORMER

	Calculation	Simulation	Experiment
L_{11} [nH]	114	113	125
L_{12}, L_{21} [nH]	56	80	69
L_{22} [nH]	243	267	264
L_s [nH]	101	89	107
L_p [nH]	243	267	264
n	4.34	3.34	3.83

III. ANALYSIS AND DESIGN OF STACKED TOROIDAL TRANSFORMER

This section discusses the fabrication scheme (Section III-A), design procedure (Section III-B), simulation

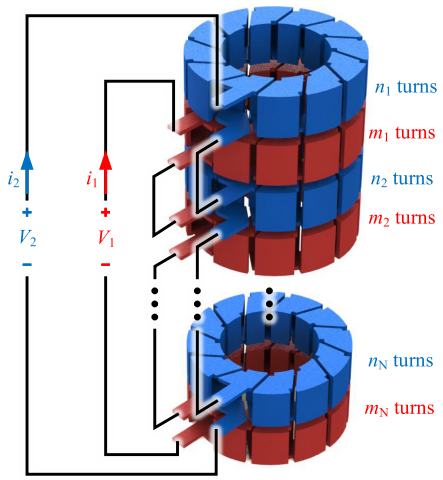

Fig. 12. Schematic drawing of the stacked toroidal transformer. The primary winding features N red toroids connected in series, each with m_i turns. The secondary winding features N blue toroids connected in series, each with n_i turns.

(Section III-C), and experimental results (Section III-D) for the stacked toroidal transformer.

Opposed to the nested structure which couples the N^2 magnetic fields of two toroids, the stacked transformer couples the one-turn magnetic fields. The N^2 fields of each toroid serve as leakage inductance for the transformer. Thus, this structure can fine-tune the leakage inductance by setting the number of turns of each individual toroid. It is also advantageous in confining the leakage fields within its body, unlike conventional wire-wound air-core transformers where leakage fields escape the structure. Fig. 12 displays a diagram for the transformer. As shown, the primary and secondary feature N toroids connected in series and are interleaved with each other throughout the stack. Each toroid has m_j turns for the primary and n_i turns for the secondary. Although it is not a requirement for the primary and secondary to maintain the same number of toroids, for this article we will uphold this symmetry for simplicity in analysis and understanding.

A. Fabrication Methodology

We fabricate the toroids similarly to the nested transformer design where each toroid is 3-D printed and electroplated to 70-μm thickness. Afterward, we soldered the tabs of each toroid onto a PCB where the board traces connect them in series. Each winding is spaced apart to prevent shorting and arcing between adjacent toroids.

B. Design Procedure

Fig. 13 displays an equivalent circuit model for the transformer, where each toroid is modeled as an N^2 inductance in series with a one-turn coupled inductor. We can further simplify the circuit by combining all series N^2 inductances into a single leakage inductance and all series one-turn coupled inductances into one coupled inductor, as denoted in Fig. 13.

Thus, the transformer design requires the calculation of three variables: the mutual inductance (L_m), the self-inductance

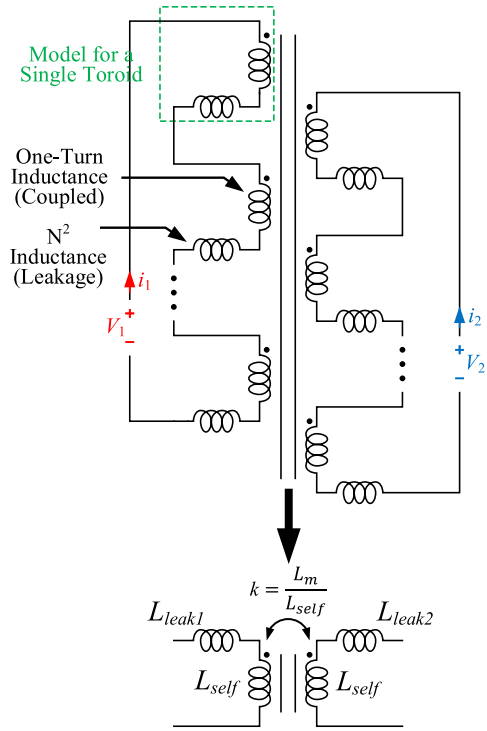

Fig. 13. Electrical equivalent model for the stacked transformer. Each toroid can be modeled as a one-turn coupled inductor in series with an additional N^2 inductor serving as leakage. This model can be simplified as two coupled inductors with two independent leakage inductances. k is the coupling coefficient between the one-turn rings of the two windings. Note that it does not account for the N^2 leakage flux, which are modeled as separate inductors.

(L_{self}), resulting from a nonunity coupling coefficient of the toroids, and the leakage inductance from the N^2 contributions (L_{leak1} and L_{leak2}). The inductance matrix expression for the stacked structure is written as

$$\begin{bmatrix} L_{11} & L_{12} \\ L_{21} & L_{22} \end{bmatrix} = \begin{bmatrix} L_{\text{self}} + L_{\text{leak1}} & L_m \\ L_m & L_{\text{self}} + L_{\text{leak2}} \end{bmatrix}. \quad (12)$$

The following sections provide algebraic formulas for the variables.

1) L_m and L_{self} Calculations: The mutual inductance resulting from the one-turn coupling of each ring is synonymous with two coupled solenoids. Furthermore, the mutual inductance is independent of the number of turns of each toroid and the outer diameter because the inner diameter constrains the magnetic field inside the barrel of the structure. Searle and Airey's formula in (13) calculates the mutual inductance of two coupled concentric solenoids with parameters labeled in Fig. 14 [45]. Dimensions are in units of cm and the inductance is in nH

$$L_m = \frac{2\pi^2 a^2 N_1 N_2}{d}\left[1 + \frac{A^2 a^2}{8\,d^4}L_2 + \frac{A^4 a^4}{32\,d^8}X_2 L_4 + \frac{A^6 a^6}{32\,d^{12}}X_4 L_6 + \frac{A^8 a^8}{32\,d^{16}}X_6 L_8 + \cdots + \frac{1}{32}\left(\frac{Aa}{d^2}\right)^{2n} X_{2n-2} L_{2n} + \ldots\right]. \quad (13)$$

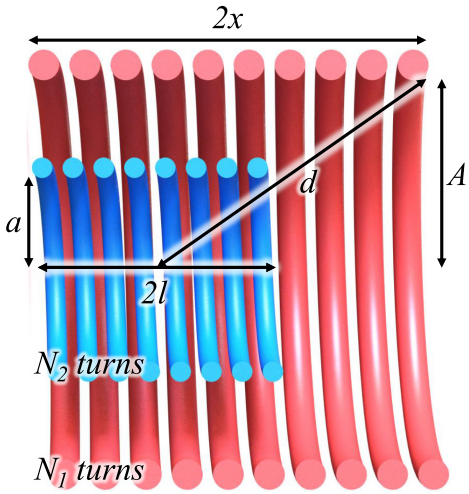

Fig. 14. Cross-sectional cutout view of two coupled uncentered concentric solenoids. A, x, and N_1 are the radius, half-length, and number of turns for the outer solenoid, respectively. a, l, and N_2 are that of the inner structure. d is the distance from the inner solenoid's center to the farthest circumferential point of the outer solenoid.

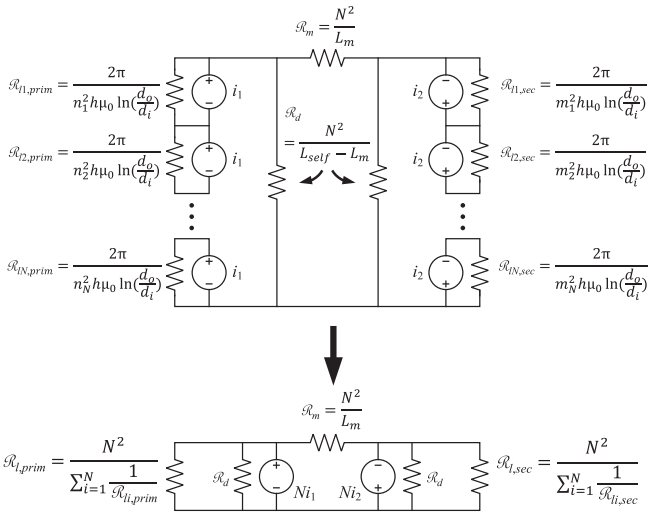

Fig. 15. Magnetic circuit model for the stacked toroid transformer. Each toroid is modeled as an MMF source in parallel with its N^2 reluctance, all coupled through the mutual reluctance $\mathcal{R}_m$. The circuit can be simplified to an equivalent model with two MMF sources.

Eqaution (14) evaluates the coefficients in Searle and Airey's equation X and L

$$
\begin{aligned}
X_2 &= 3 - 4\frac{x^2}{A^2} \\
X_4 &= \frac{5}{2} - 10\frac{x^2}{A^2} + 4\frac{x^4}{A^4} \\
X_6 &= \frac{35}{16} - \frac{35}{2}\frac{x^2}{A^2} + 21\frac{x^4}{A^4} - 4\frac{x^6}{A^6} \\
L_2 &= 3 - 4\frac{l^2}{a^2} \\
L_4 &= 5/2 - 10\frac{l^2}{a^2} + 4\frac{l^4}{a^4} \\
L_6 &= \frac{35}{16} - \frac{35}{2}\frac{l^2}{a^2} + 21\frac{l^4}{a^4} - 4\frac{l^6}{a^6} \\
L_8 &= \frac{63}{32} - \frac{105}{4}\frac{l^2}{a^2} + 63\frac{l^4}{a^4} - 36\frac{l^6}{a^6} + 4\frac{l^8}{a^8}.
\end{aligned} \tag{14}
$$

The benefit of this analytic method is that Searle and Airey's equation can estimate the mutual inductance algebraically, using just geometric parameters, without the necessity of elliptic integrals. While other formulas that cal Note that for our case the primary and secondary are symmetric, meaning they have the same number of toroids, all with the same dimensions and spaced evenly apart. This allows (13) to be simplified by setting the conditions in (15), where g is the separation between neighboring toroids, and h is the height of each toroid

$$N_1 = N_2,\ A = a,\ l = x,\ d = \sqrt{A^2 + (x + h + g)^2}. \tag{15}$$

Additionally, Searle and Airey's formula also calculates the self-inductance by imposing the condition where the two solenoids are perfectly aligned since the self-inductance equates to the mutual inductance when the solenoids have ideal coupling. Searle and Airey's formula in (13) determines the self-inductance by setting $d = \sqrt{A^2 + x^2}$ as

$$L_{\text{self}} = L_m|_{k=1},\ d = \sqrt{A^2 + x^2}. \tag{16}$$

2) Leakage Inductance Calculation: The turns introduced to each toroid produce the leakage inductance of the transformer. Therefore, the primary and secondary leakages are simply the summation of the N^2 inductance of each toroid, as shown in (17). The term inside the summation formulates the inductance for a toroid with a square cross section. d_o, d_i, and h are the outer diameter, inner diameter, and height of each toroid, respectively. All variables in (17) are represented in the International System of Units (SI) form

$$
\begin{aligned}
L_{\text{leak1}} &= \sum_{k=1}^{N} \frac{n_k^2 h\mu_0}{2\pi} \ln\left(\frac{d_o}{d_i}\right) \\
L_{\text{leak2}} &= \sum_{k=1}^{N} \frac{m_k^2 h\mu_0}{2\pi} \ln\left(\frac{d_o}{d_i}\right).
\end{aligned} \tag{17}
$$

3) Magnetic Circuit Model: To derive an equivalent magnetic circuit model for the transformer, each toroid can be represented as a magnetomotive force (MMF) source in parallel with an N^2 reluctance serving as the leakage produced by the turns introduced to the toroid shown in Fig. 15. As explained in the leakage inductance calculation section, each toroid has an N^2 inductance described by (17); therefore, the leakage reluctance is the inverse of the N^2 inductance. Note that the reluctance is a function of n, and not N. Each source-reluctance branch is in series because the one-turn flux produced by each toroid is coupled. Therefore, the flux from each MMF source is equivalent to the sum of the coupled one-turn flux and the leakage N^2 flux. $\mathcal{R}_m$ is the reluctance corresponding to the mutual flux path from

TABLE VI
LIST OF PARAMETERS FOR STACKED TRANSFORMER DESIGN EXAMPLE

	Primary	Secondary
Outer diameter [mm]	30	
Inner diameter [mm]	16	
Height [mm]	4	
Thickness [mm]	1.5	
Separation distance [mm]	2	
Number of turns	4,4,4,6,6	7,9,9,9,9

the one-turn coupling. The additional $\mathcal{R}_d$ reluctances result from incomplete coupling between the primary and secondary toroids.

To relate the magnetic circuit model to the inductance matrix, the magnetic circuit should be simplified to two single MMF sources representing the primary and secondary currents. To conjoin the parallel reluctance-source branches into an equivalent model, we develop the Thevenin equivalent circuit for the branches, which is a single source of Ni_1 for the primary and Ni_2 for the secondary. This maintains proper current-flux relationships with the rest of the connected circuit but neglects the various leakage reluctances $\mathcal{R}_{li,\text{prim}}$ and $\mathcal{R}_{li,\text{sec}}$. Therefore, we also include in parallel to the sources equivalent reluctances $\mathcal{R}_{l,\text{prim}}$ and $\mathcal{R}_{l,\text{sec}}$ that model the effects of the individual parallel leakage reluctances. To combine the parallel leakage reluctances, $\mathcal{R}_{l,\text{prim}}$ and $\mathcal{R}_{l,\text{sec}}$ should have the same power as the sum of all of the parallel leakage reluctances as determined from

$$\frac{(Ni)^2}{\mathcal{R}_l} = \sum_{k=1}^{N} \frac{i^2}{\mathcal{R}_{li}} \;\rightarrow\; \mathcal{R}_l = \frac{2\pi N^2}{h\mu_0 \ln\left(\frac{d_o}{d_i}\right) \sum_{i=1}^{N} n_i^2}$$
$$\text{where } \mathcal{R}_{li} = \frac{2\pi}{n_i^2\, h\mu_0 \ln\left(\frac{d_o}{d_i}\right)}. \tag{18}$$

The inductance matrix in terms of the number of toroids N and the reluctance values is written as

$$\begin{bmatrix} L_{11} & L_{12} \\ L_{21} & L_{22} \end{bmatrix} = \begin{bmatrix} \frac{N^2}{\mathcal{R}_m \| \mathcal{R}_d \| \mathcal{R}_{l,\text{prim}}} & \frac{N^2}{\mathcal{R}_m} \\ \frac{N^2}{\mathcal{R}_m} & \frac{N^2}{\mathcal{R}_m \| \mathcal{R}_d \| \mathcal{R}_{l,\text{sec}}} \end{bmatrix}. \tag{19}$$

The inductance matrix in (19) is equivalent to (12).

4) Design Example: For demonstration, we select to design a transformer with five toroids for the primary and five for the secondary. Table VI lists the physical parameters for the ten toroids. To start with calculating L_m, we follow (13) and set the parameters of a, A, d, l, x, N_1, and N_2 based on the values listed in Table VI. Equation (14) obtains the X and L constants necessary for the calculation. To obtain the values of a and A, we subtract the thickness of the structure from the inner diameter giving a more realistic hole radius. Similarly for x and l, we account for the toroid's thickness by adding 1.5 mm to the total length of the structure

$$N_1 = N_2 = 5,\; a = A = \frac{16\,\text{mm} - 1.5\,\text{mm}}{2} = 7.25\,\text{mm}$$
$$x = l = \big[4\,\text{mm} \times (N_1 + N_2 - 1) +$$
$$2\,\text{mm} \times (N_1 + N_2 - 2) + 1.5\,\text{mm}\big]/2 = 26.75\,\text{mm}$$
$$d = \sqrt{7.25^2 + (22.75 + 4 + 1)^2} = 33.54\,\text{mm}. \tag{20}$$

TABLE VII
LIST OF IMPEDANCES AT 20 MHz DERIVED FROM COMSOL SIMULATION OF THE EXAMPLE STACKED TRANSFORMER AND THE CALCULATED INDUCTANCE MATRIX PARAMETERS FROM THE IMPEDANCES

Parameter	Value
$\hat{V_1}/\hat{i_1}$ [Ω], 1 A in primary	$0.103 + 21.677j$
$\hat{V_1}/\hat{i_1}$ [Ω], 1 A in primary and secondary	$0.130 + 32.121j$
$\hat{V_2}/\hat{i_2}$ [Ω], 1 A in primary and secondary	$0.220 + 42.543j$
L_{11} [nH]	172
L_{12}, L_{21} [nH]	83
L_{22} [nH]	255

Based on the calculation, we obtain a final value of 76 nH for L_m. For L_{self}, we follow the same equation except that d changes to the expression in (16) with a value of 27.72 mm. The result for L_{self} is 87 nH. Lastly, to obtain the leakage inductances L_{leak1} and L_{leak2}, we follow (17) by summing the N^2 inductances of all 5 toroids for each winding. The n and m values equate to the number of turns listed in Table VI. h is the height of the toroid, which is 4 mm, d_o and d_i are 30 and 16 mm, respectively. Therefore, L_{leak1} results in 60 nH and L_{leak2} results in 188 nH. Lastly, $L_{11} = L_{\text{self}} + L_{\text{leak1}}$ and $L_{22} = L_{\text{self}} + L_{\text{leak2}}$ which concludes to $L_{11} = 147$ and $L_{22} = 275$ nH.

Second, to obtain the magnetic circuit values, we can follow the equations in Fig. 15 and (18) to obtain the reluctances as

$$\mathcal{R}_m = \frac{5^2}{76\,\text{nH}} = 3.29 \times 10^8, \text{H}^{-1}$$
$$\mathcal{R}_d = \frac{5^2}{(87 - 76)\,\text{nH}} = 2.27 \times 10^9,\ \text{H}^{-1}$$
$$\mathcal{R}_{l,\text{prim}} = \frac{2\pi(5^2)}{(4\,\text{mm}) \times \ldots \; (4\pi \times 10^{-7}) \times \ldots \; \left(\ln\left(\frac{30\,\text{mm}}{16\,\text{mm}}\right)\right) \times \ldots \; (7^2 + 4 \times 9^2)} = 4.14 \times 10^8, \text{H}^{-1}$$
$$\mathcal{R}_{l,\text{sec}} = \frac{2\pi(5^2)}{(4\,\text{mm}) \times \left(4\pi \times 10^{-7}\right) \times \ldots \; \left(\ln\left(\frac{30\,\text{mm}}{16\,\text{mm}}\right)\right) \times \left(7^2 + 4 \times 9^2\right)} = 1.33 \times 10^8, \text{H}^{-1}. \tag{21}$$

To verify, we can calculate $L_{11} = \frac{N^2}{\mathcal{R}_m \| \mathcal{R}_d \| \mathcal{R}_{l,\text{prim}}}$ as 147 nH, $L_{22} = \frac{N^2}{\mathcal{R}_m \| \mathcal{R}_d \| \mathcal{R}_{l,\text{sec}}}$ as 275 nH and $L_m = \frac{N^2}{\mathcal{R}_m}$ as 76 nH, which matches the previously calculated inductance matrix. The final calculated, simulated, and measured inductance matrix values for this design are listed and compared in Table IX in Section III-D.

TABLE VIII
MEASURED VALUES OF THE STACKED TRANSFORMER SHOWN IN Fig. 17

Parameter	Value
$L_{1,\text{open}}$ [nH]	185
$L_{2,\text{open}}$ [nH]	262
$L_{2,\text{short}}$ [nH]	222
L_{11} [nH]	185
L_{12}, L_{21} [nH]	86
L_{22} [nH]	262

Second half of the table lists the inductance matrix parameters derived from the measured values.

TABLE IX
COMPARISON OF INDUCTANCE MATRIX VALUES AND CANTILEVER PARAMETERS (L_s, L_p, n) BETWEEN FIRST-ORDER CALCULATIONS, COMSOL SIMULATION, AND EXPERIMENTALLY BUILT STACKED TRANSFORMER

	Calculation	Simulation	Experiment
L_{11} [nH]	147	172	185
L_{12}, L_{21} [nH]	76	83	86
L_{22} [nH]	275	255	262
L_s [nH]	127	145	157
L_p [nH]	275	255	262
n	3.67	3.07	3.05

C. Simulation Results

Based on the design parameters listed in Table VI, we simulate the structure in COMSOL. The procedure to extract the inductance matrix is previously explained in Section II-C. Similarly, two simulations are necessary to obtain the inductance matrix. The first simulation is with 1-A current injected into the primary, and the second is with 1 A current injected into both windings, with a frequency of interest at 20 MHz. Fig. 16 provides images of the H-field magnitude from the two simulations.

Notice in Fig. 16(b) that the H-field intensity in the cross section of each toroid is different throughout the stack, where cross sections of toroids with a greater number of turns have higher peak field intensity, leading to more leakage inductance. Therefore, our method of design demonstrates the capability to control leakage fields through varying the number of turns, where toroids with a greater number of turns have larger N^2 magnetic field intensities. Also, the structure can confine the N^2 leakage field within the toroidal structure, which is an advantage over conventional transformer structures where leakage fields are compensated through separate inductors in series with the transformer. Table VII lists the inductance results obtained from COMSOL simulation and the Table IX compares them with the calculated and experimental values.

D. Experimental Results

We experimentally validated our transformer design by constructing a stacked transformer with physical parameters listed in Table VI. Fig. 17 shows the transformer built from the design example.

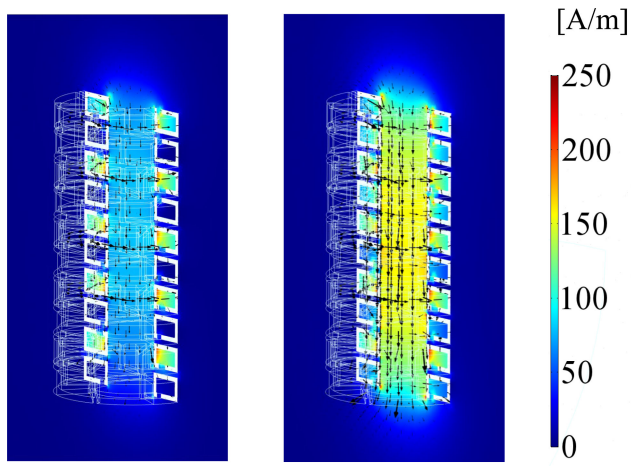

Fig. 16. (a) H-field colormap (in units of A/m) of the structure's vertical cross section with Lumped Port 1's current set as 1 A. (b) H-field colormap of the structure with Lumped Port 1 and Lumped Port 2's current set as 1 A. Notice that field densities are more intense inside cross sections of toroids with more turns.

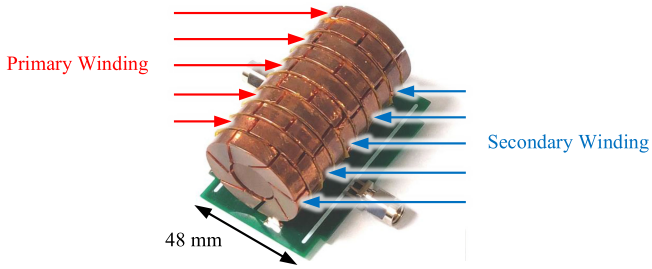

Fig. 17. Photograph of 5 toroid primary and secondary transformer with parameters listed in Table VI. The red arrows point to the primary toroids connected in series, and the blue arrows point to the secondary toroids.

We followed the inductance matrix measurement procedure similar to the nested transformer measurement procedure, which is explained in Section II-D. Table VIII lists the experimentally measured inductances and the inductance matrix parameters. Lastly, Table IX compares the inductance matrix values and cantilever model values between experiment, simulation, and calculation. We observe good agreement between the three, hence verifying our design methodology.

IV. ANALYSIS AND DESIGN OF INTERLEAVED TRANSFORMER

Third, we demonstrate the interleaved transformer which features two parallel windings wound together along the same path.

A. Fabrication Methodology

The interleaved transformer features two parallel windings looped in a side-by-side fashion around a toroid. Compared to the previous two transformers, the interleaved structure has the

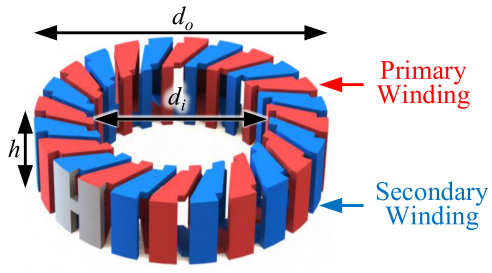

Fig. 18. Two-winding interleaved transformer structure with the two separate windings colored in red and blue.

simplest fabrication process, requiring only a single 3-D printed piece and no assembly procedure. Fig. 18 displays the diagram of the 3-D printed scaffold for the interleaved transformer.

The red and blue colors represent the two distinct windings. The windings are separated by a gap distance for voltage isolation requirements. The gray H-bar structure is unplated and maintains the structural robustness of the windings. This can be achieved either by masking the H-bar region before plating to selectively plate only the windings, or done postplating by either selectively etching or cutting away the copper film layer on the H-bar. Similar to the other structures, the plating thickness is between 50 and 70 μm, which is twice the skin depth of copper at 10 MHz.

B. Design Methodology

Due to manufacturing constraints, both windings share the same number of turns as well as the same geometric parameters, meaning the transformer's inductance matrix is symmetric as

$$\begin{bmatrix} L_{11} & L_{12} \\ L_{21} & L_{22} \end{bmatrix} = \begin{bmatrix} L_{\text{self}} & L_m \\ L_m & L_{\text{self}} \end{bmatrix} = \begin{bmatrix} 1 & k \\ k & 1 \end{bmatrix} L_{\text{self}}. \tag{22}$$

Equation (23) calculates the self-inductance L_{self}. This equation is equivalent to the toroidal inductor's formula, as described in [31], since each winding is structurally identical to a toroidal inductor

$$L_{\text{self}} = \frac{N^2 h \mu_0}{2\pi} \ln\left(\frac{d_o}{d_i}\right) + \frac{d_i + d_o}{4} \mu_0 \left[\ln\left(8\frac{d_o + d_i}{d_o - d_i}\right) - 2\right]. \tag{23}$$

While the interleaved transformer is simple to fabricate, developing closed-form equations for the mutual inductance involves difficult calculations. Due to the angular offset between the adjacent turns of each winding, the magnetic dipole of each turn of each winding does not completely align, which leads to nonunity coupling. The mutual inductance is a fraction of the self-inductance through $L_m = kL_{\text{self}}$, where the constant k is the coupling coefficient. The coupling coefficient primarily is determined by the ratio of the inner and outer diameters d_i/d_o and the number of turns N. Therefore to design for a target mutual inductance, we can typically assume an initial coupling coefficient between 0.6 and 0.8. This initial selection for the coupling coefficient is based on design intuition and is reasonable for designs seeking to achieve the highest possible coupling. Using these initial values, we can run finite-element method (FEM) simulations to retrieve the exact inductance matrix and iteratively adjust the physical parameters through multiple resimulations.

Additionally, the interleaved transformer has limitations in the selection of its inductance matrix. Other than upholding a symmetric inductance matrix, circuit designers cannot freely adjust the leakage inductance of the transformer, requiring additional compensation inductors on the primary and secondary to achieve the desired inductance matrix.

1) Design Example: To provide an example, we design an interleaved transformer with specifications listed in Table X.

TABLE X
LIST OF PARAMETERS FOR THE EXAMPLE INTERLEAVED TRANSFORMER DESIGN EXAMPLE

Parameter	Value
Outer diameter [mm]	37
Inner diameter [mm]	24
Height [mm]	12.5
Thickness [mm]	1
Separation distance [mm]	1
Number of turns per winding	10

With these values, we use (23) to obtain an L_{self} of 139 nH. Next, we approximate the mutual inductance by assuming a coupling coefficient of 0.7, resulting in $L_m = 98$ nH. The calculated inductance matrix is written as

$$\begin{bmatrix} L_{11} & L_{12} \\ L_{21} & L_{22} \end{bmatrix} = \begin{bmatrix} 139\,\text{nH} & 98\,\text{nH} \\ 98\,\text{nH} & 139\,\text{nH} \end{bmatrix}. \tag{24}$$

Table XIII in Section IV-D compares these initial values with simulation and experimental results.

C. Simulation Results

Similar to the previous transformers, we verify our design using FEM simulation. Section II-C explains the procedure to extract the inductance matrix from COMSOL. Fig. 19 displays the H-field simulations of the transformer. Note that the field distribution of this transformer design is similar to that of a toroidal inductor exemplified in [40]. We ran two simulations to obtain the inductance matrix, one with 1 A injected into the primary winding and the other with 1 A injected into both windings at 20 MHz. The first simulation directly provides the impedance associated with L_{11} while the second simulation provides the impedance associated with $L_{11} + L_m$ and $L_{22} + L_m$. Table XI provides the simulation results and inductance matrix values.

D. Experimental Results

Lastly, we fabricate the example interleaved transformer using the outlined fabrication procedure. Fig. 20 shows the image of the ten turns interleaved transformer. To achieve similar inductance matrix to the nested and stacked transformers, we added additional compensation inductors to the primary and secondary side to increase the self-inductances. The primary inductor has a value of 27 nH and the secondary compensation

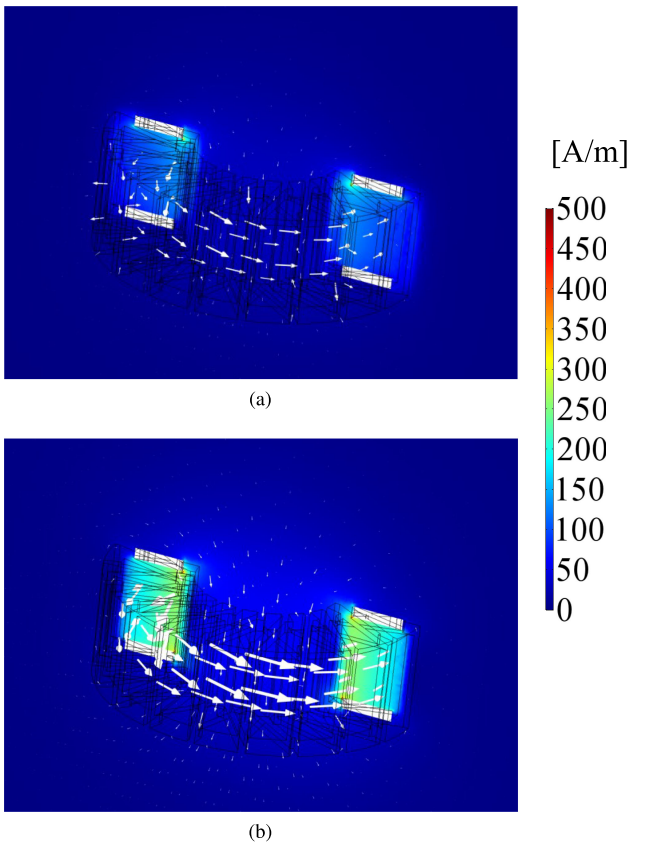

Fig. 19. (a) H-field magnitude of the interleaved transformer with 1-A, 20-MHz current injected into the primary winding. White arrows correspond to the 3-D spatial directions of the H-field. The legend is in units of A/m. (b) H-field magnitude of the interleaved transformer with 1-A, 20-MHz current injected into both windings.

TABLE XI
LIST OF IMPEDANCES AT 20 MHz, DERIVED FROM COMSOL SIMULATION OF THE EXAMPLE INTERLEAVED TRANSFORMER AS WELL AS CALCULATED INDUCTANCE MATRIX PARAMETERS FROM THE IMPEDANCES

Parameter	Value
$\hat{V_1}/\hat{i_1}$ [Ω], 1 A in primary	$0.101 + 17.331j$
$\hat{V_1}/\hat{i_1}$ [Ω], 1 A in primary and secondary	$0.113 + 27.801j$
$\hat{V_2}/\hat{i_2}$ [Ω], 1 A in primary and secondary	$0.113 + 27.801j$
L_{11} [nH]	138
L_{12}, L_{21} [nH]	83
L_{22} [nH]	138

inductor has a value of 137 nH. Both of these values are deducted from the inductance matrix in Table XIII when comparing the values between calculation, simulation, and experimental measurement.

We followed the same measurement procedure and calibration technique using the impedance analyzer similar to the previous sections. Table XII lists the measured values before deducting the compensation inductor values.

Furthermore, Table XIII compares the values between calculation, simulation, and experimental measurement for the inductance matrix and cantilever parameters. The self-inductance

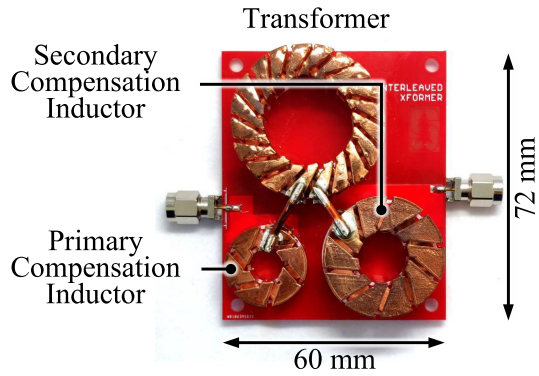

Fig. 20. Photograph of the fabricated interleaved transformer connected to the compensation inductors on the circuit board.

TABLE XII
MEASURED VALUES OF THE INTERLEAVED TRANSFORMER SHOWN IN Fig. 20 INCLUDING THE COMPENSATION INDUCTORS AS WELL

Parameter	Value
$L_{1,\text{open}}$ [nH]	164
$L_{2,\text{open}}$ [nH]	279
$L_{2,\text{short}}$ [nH]	239
L_{11} [nH]	164
L_{12}, L_{21} [nH]	81
L_{22} [nH]	279

Second half of the table lists the inductance matrix parameters derived from the measured values.

TABLE XIII
COMPARISON OF INDUCTANCE MATRIX VALUES AND CANTILEVER PARAMETERS (L_s, L_p, n) BETWEEN FIRST-ORDER CALCULATIONS, COMSOL SIMULATION, AND EXPERIMENTALLY BUILT INTERLEAVED TRANSFORMER

	Calculation	Simulation	Experiment
L_{11} [nH]	139	138	137
L_{12}, L_{21} [nH]	98	83	81
L_{22} [nH]	139	138	142
L_s [nH]	70	88	91
L_p [nH]	139	138	142
n	1.42	1.66	1.75

L_{11} and L_{22} agree well among the three methods. For the mutual inductance L_m, the simulation result agrees well with the experiment, which demonstrates the proper fabrication of the structure. However, the calculated L_m has a 20% difference compared to the experimental design, which is reasonable since the calculated L_m results from a speculated coupling coefficient.

V. TRANSFORMER LOSS ANALYSIS AND COMPARISON

Following the explanation in [46], the transformer's equivalent winding loss circuit in Fig. 21 is a simple method to express the transformer's power dissipation, and the total power loss

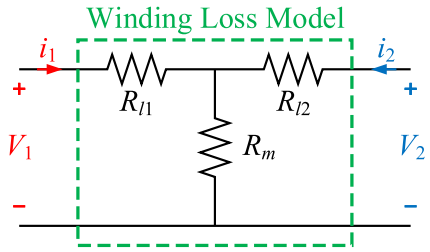

Fig. 21. Equivalent 2-port winding loss circuit model that is used to obtain the resistance matrix of the transformer.

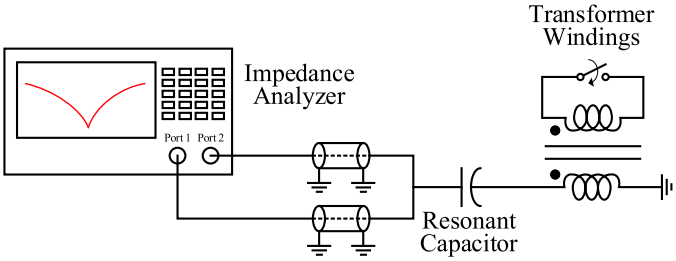

Fig. 22. Diagram of the shunt-through method used to accurately measure the resistive component of the transformer at a fixed frequency.

based on the circuit model is calculated as

$$\langle P_{\text{avg}} \rangle = \frac{1}{2}(R_{l1} + R_m)\hat{i}_1\hat{i}_1^* + \frac{1}{2}(R_{l2} + R_m)\hat{i}_2\hat{i}_2^* + \frac{1}{2}(R_m)(\hat{i}_1\hat{i}_2^* + \hat{i}_1^*\hat{i}_2). \tag{25}$$

$$\begin{bmatrix}\hat{V}_1 \\ \hat{V}_2\end{bmatrix} = \begin{bmatrix}R_{11} & R_m \\ R_m & R_{22}\end{bmatrix}\begin{bmatrix}\hat{i}_1 \\ \hat{i}_2\end{bmatrix} = \begin{bmatrix}R_{l1} + R_m & R_m \\ R_m & R_{l2} + R_m\end{bmatrix}\begin{bmatrix}\hat{i}_1 \\ \hat{i}_2\end{bmatrix}. \tag{26}$$

Furthermore, (26) develops the *I–V* relationship for the winding loss circuit, where similar to the inductance matrix, the losses of the transformer can be represented by a two-port resistance matrix. Because the ac resistances of the transformers are on the order 100 mΩ, measuring the one-port reflection using an impedance analyzer does not accurately obtain the resistance matrix.

A. Shunt-Through Measurement Technique

According to Keysight's impedance analysis application note [47], measuring impedances under 1 Ω results in over 10% error when using the standard one-port reflection technique. However, the shunt-through configuration is capable of resolving impedances on the order of 100 mΩ. To set up the measurement, the impedance analyzer is calibrated to measure a 2-port system where, both ports are calibrated using the Keysight 85052D calibration kit using an open, short, and 50-Ω broadband load. Then, an SMA T-adapter connects the two ports for the through calibration. Once calibrated, the impedance analyzer measures the device-under-test with both ports shorted together. Fig. 22 displays a schematic diagram of the measurement test setup.

TABLE XIV
DIMENSIONS AND INDUCTANCE MATRIX VALUES OF THE REFERENCE COPPER FOIL-WOUND TRANSFORMER SHOWN IN FIG. 23

Parameter	Transformer	Compensation inductor
Outer diameter [mm]	47	24
Inner diameter [mm]	25	14
Height [mm]	18.5	8.5
Foil width [mm]	5	3
Turns	5 (per winding)	8
Foil thickness [μm]	70	70
L_{11} [nH]	184	
L_{12}, L_{21} [nH]	74	
L_{22} [nH]	287	

Furthermore, to measure the transformer's equivalent series resistance (ESR), we connect a capacitor in series with the winding to resonate at the frequency of interest. The purpose of this is that directly measuring the real component for the impedance requires accurate knowledge of the phase, especially since the real component is only a small fraction of the total impedance. At the resonant frequency, the inductive and capacitive components of the LC cancels and the minimum of the magnitude of the impedance is the ESR. Although this measurement technique also includes the ESR of the capacitor, we neglect this impact on our measurement. For our measurements, we use capacitors from American Technical Ceramics (ATC) RF/Microwave Design Kit which features Q factors $>$ 10 000 at 1 MHz for values between 0.1 and 200 pF [48]. Extrapolating the Q factor for our frequency of interest at 30 MHz, the series resistance for a 100 pF capacitor is 16 mΩ, which is below the resolution of the measurement setup and hence negligible. Furthermore, we also utilize multiple capacitors in parallel which further reduces the capacitor ESR.

B. Q Factor Measurement Technique

Also, we verify the results from the shunt-through method by measuring the Q factor of the LC network from Fig. 22 and using (27) to solve for the inductive ESR

$$\text{ESR} = \frac{\omega L}{Q} = \frac{\text{Im}\{Z\}}{Q},\ Q = \frac{f_o}{\Delta f_{3\,\text{dB}}}. \tag{27}$$

To measure the Q factor, we record the resonant frequency and divide this value by the 3-dB bandwidth or when the phase of the impedance becomes ±45°. While this method does require an accurate measurement of the phase, we utilize this as a supplementary evaluation to validate the result from the shunt-through measurement.

Because the transformer's resistance matrix has three unknown values, we perform each measurement three times per transformer. For the first measurement, we obtain the ESR of the primary coil with the secondary open providing $R_{l1} + R_m$. Second, we measure the resistance of the secondary with the primary open giving $R_{l2} + R_m$. Lastly, we obtain the resistance of the secondary with the primary shorted which provides $R_{l1}||R_m + R_{l2}$. Table XV lists the measured values from both methods for the three transformers demonstrated in this article

TABLE XV
LIST OF MEASURED RESISTANCE MATRIX VALUES AT 30 MHZ FOR THE TRANSFORMERS USING THE SHUNT-THROUGH MEASUREMENT METHOD AND Q FACTOR METHOD; CALCULATED RESISTANCE MATRIX VALUES FROM THE SHUNT-THROUGH METHOD; CALCULATED Q FACTORS FOR THE PRIMARY AND SECONDARY WINDINGS AT 30 MHZ WITHOUT COMPENSATION INDUCTORS; CYLINDRICAL VOLUMES OF THE TRANSFORMERS WITHOUT COMPENSATION INDUCTORS

Shunt-through method	Nested	Stacked	Interleaved	Foil-wound
$R_{l1}+R_m$ [mΩ]	317	322	300	409
$R_{l2}+R_m$ [mΩ]	1260	510	603	644
$R_{l1}\|\|R_m+R_{l2}$ [mΩ]	1140	472	578	634
Q Factor method	Nested	Stacked	Interleaved	Foil-wound
$R_{l1}+R_m$ [mΩ]	295	296	286	393
$R_{l2}+R_m$ [mΩ]	1150	454	537	592
$R_{l1}\|\|R_m+R_{l2}$ [mΩ]	1060	464	531	615
Resistance matrix	Nested	Stacked	Interleaved	Foil-wound
R_{l1} [mΩ]	122	212	213	345
R_m [mΩ]	195	110	87	64
R_{l2} [mΩ]	1065	400	444	580
Q Factor ($\frac{\omega L}{R}$)	Nested	Stacked	Interleaved	Foil-wound
Primary winding	74	108	108	85
Secondary winding	39	97	107	92
Volume [cm^3]	Nested	Stacked	Interleaved	Foil-wound
	17.2	46.4	15.3	32.1

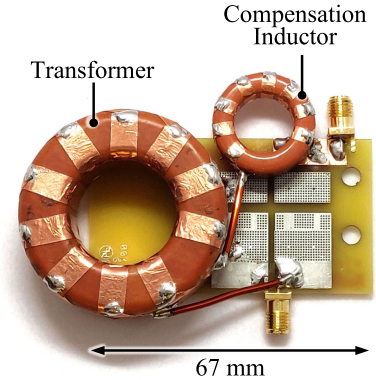

Fig. 23. Image of the reference copper foil-wound transformer used to compare with the 3-D printed examples. The foil is wound around two plastic cores. The large toroid features two five-turn windings interleaved to form the transformer. The smaller toroid is an eight-turn inductor used to increase the leakage inductance at the secondary side to achieve comparable inductance matrices.

as well as the transformer's resistance matrix calculated using the shunt-through measurement technique at 30 MHz.

To compare the printed transformers with a conventional option, Fig. 23 shows a reference transformer constructed using copper foil wound around plastic toroidal cores. According to [31] and [19], the current state-of-the-art toroidal windings are made with foil due to the large surface area to help mitigate skin effect losses. To achieve a fair comparison, the reference foil-wound transformer exhibits approximately the same size to the 3-D printed components as well as equal inductance matrices. Additionally, the minimum separation between adjacent turns is 1.5 mm, equivalent to the 3-D printed components.

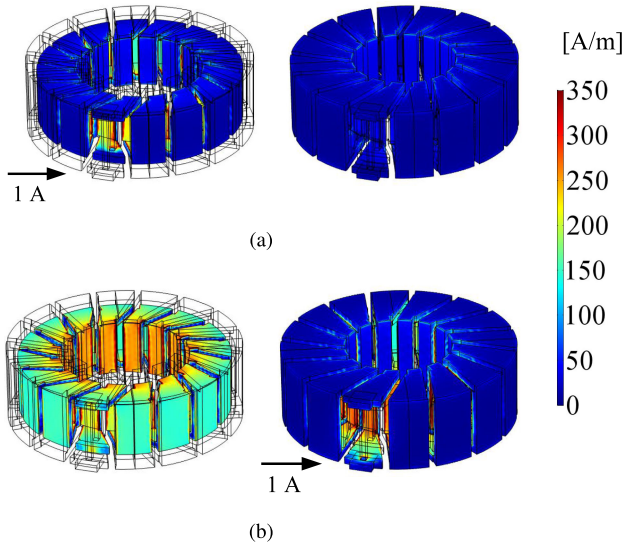

Fig. 24. Surface current density of the inner winding (left figure) and outer winding (right figure) for when a (a) 1-A, 20-MHz current is injected into the inner winding and when a (b) 1-A, 20-MHz current is injected into the outer winding. The surface current density colormap is in units of A/m since it represents the current on the boundary of the winding. Notice that in (b), even though current is only injected into the outer winding, a large density of eddy current is introduced into the inner winding, contributing to a large resistance at the outer. In both simulations, the noninjected winding is left open, meaning the eddy current losses at the inner winding in (b) is captured by R_{l2} of the nested transformer.

Thus, to maximize the copper coverage we selected the widest available foils to wind the plastic cores while maintaining the 1.5-mm separation. Using the measurement methods discussed previously, the dimensions and inductance matrix of the foil-wound transformer is listed in Table XIV and the resistance matrix values and measurements are listed in Table XV. From Table XV, the 3-D printed transformers, other than the nested transformer, achieve similar resistance values compared to the foil-wound example, exemplifying that the proposed fabrication techniques are capable of performing on par with conventional high-frequency magnetics. In fact, at 30 MHz, the stacked and interleaved transformer have slightly lower resistances compared to the reference, likely because the copper foil has less coverage at the outer perimeter of the toroid. For all transformers, the secondary winding resistance is larger than the primary resistance, which is reasonable since the secondary windings have higher inductances than the primaries. However, for the nested transformer, R_{l2} is almost ten times higher than R_{l1}. This is contributed by two factors. First, we used sterling silver 3-D printed structures for the secondary winding, which according to [40] has 37% the conductivity of pure copper. Additionally, the secondary has many solder joints to connect the pieces to the PCB, further increasing the resistance. Second, because the primary is in flux path of the secondary, the secondary will excite eddy currents in the primary winding as shown in Fig. 24, where a large current density exists on the primary winding when the secondary is injected with current. Therefore, the combination of proximity effect and high-resistance materials degrade the performance of the secondary of the nested transformer. While

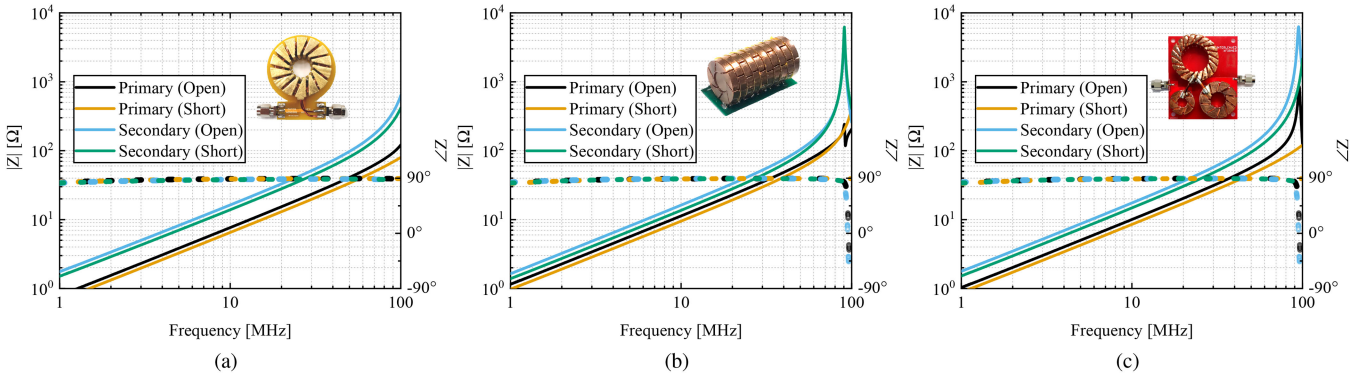

Fig. 25. Plot of the magnitude (in solid line) and phase (in dotted line) of the impedance of (a) the nested transformer, (b) the stacked transformer, and (c) the interleaved transformer at the primary with the secondary open (in black) and shorted (in orange) and at the secondary with the primary open (in blue) and the shorted (in green). These figures indicate that the SRF of the transformer is well beyond the frequencies of target applications in 10–50 MHz.

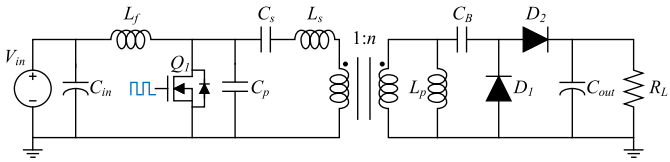

Fig. 26. Schematic of isolated 48–200 V dc–dc converter switching at 30 MHz. The circuit features a class-E inverter topology driving a transformer matching stage shown in cantilever form (highlighted in gray), and a class-DE rectifier.

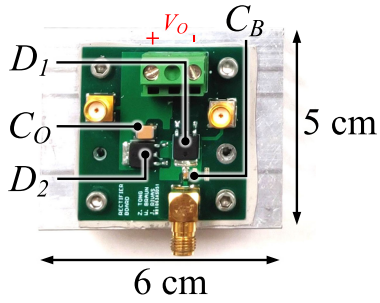

Fig. 27. Photograph of the class-DE rectifier circuit board with components labeled.

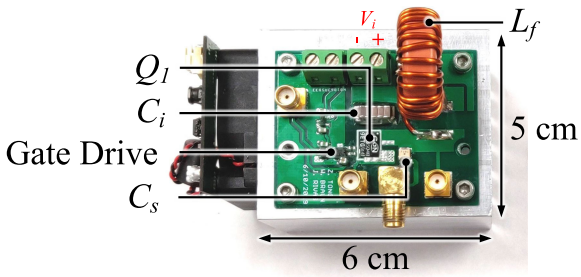

Fig. 28. Photograph of the class-E inverter circuit board with components labeled.

the interleaved and foil-wound transformers also include compensation inductors to equate the inductance matrices to the other designs, Table XV also compares the four transformers through the primary and secondary windings' Q factor without compensation inductors. These values are a function of the ratio of the windings' self-inductance (L_{11} and L_{22}) to the self-resistance ($R_{l1} + R_m$ and $R_{l2} + R_m$).

In air-core magnetics, the only method for power loss is from skin and proximity effect from the windings. Therefore, the resistances of the transformers scale with the square root of frequency, which is shown in [31], as long as the frequency is below the self-resonant frequency (SRF) of the transformer, where the inductances resonate with the parasitic capacitances. The applications of concern discussed in this article primarily target frequencies between 10 and 50 MHz. As shown in Fig. 25, the SRF's of the transformers at the various ports are at or beyond 100 MHz, meaning the transformer designs operate inductively in the frequencies of interest.

VI. Converter Demonstrations

To demonstrate the power conversion capability and performance of the transformer, we constructed a 48–200 V, 100 W resonant converter implementing a class-E inverter and class-DE rectifier. The switching frequency of the dc–dc system is 30 MHz. Fig. 26 displays the schematic of the converter.

The design of this converter is best understood when using the cantilever model representation of the transformer. This is because the rectifier can utilize the transformer's shunt secondary inductance L_p to achieve resonance. Additionally, the series primary inductance L_s serves as the class-E inverter's load inductance.

We first start with the rectifier design to achieve a resistive input impedance at the switching frequency. In LTSpice simulation, we iteratively adjusted the input shunt inductance of the rectifier until the fundamental component of the input voltage and the input current achieves a 0° phase shift. For this design, the desired L_p equates to 280 nH, leading to a rectifier impedance of 79 Ω at 30 MHz with 100 W delivered output power. Fig. 27 shows an image of the rectifier board.

Furthermore, we designed a class-E inverter with a dc choke inductor, following the design guidelines from [49]. The value of L_f is large enough such that the input current is dc. We select L_f between 5 and 10 times the value of L_s. To achieve zero voltage

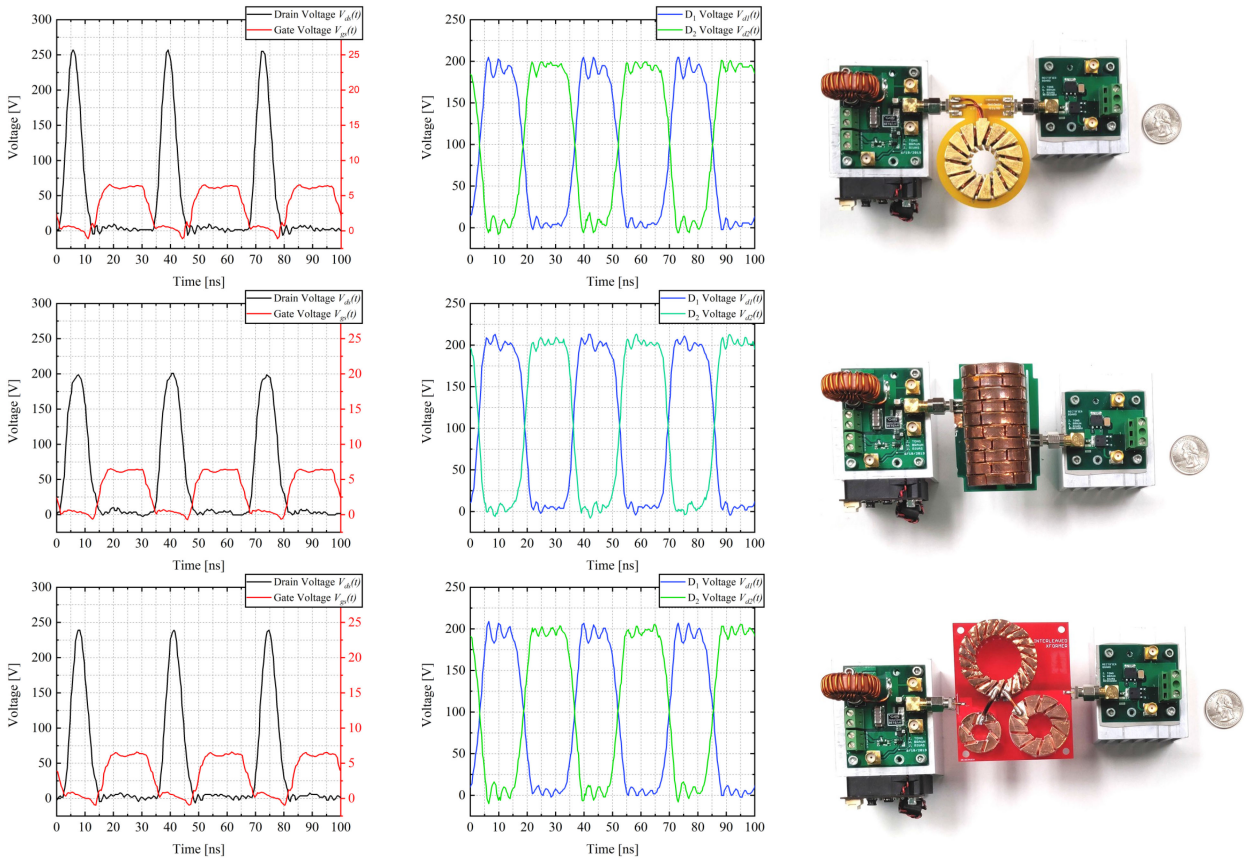

(a) (b) (c)

Fig. 29. (a) Measured drain and gate waveforms of the inverter, (b) diode waveforms of the rectifier, and (c) photographs of the full systems implementing (from top to bottom) the nested transformer, stacked transformer, and interleaved 3-D printed transformer.

switching (ZVS), the C_{oss} output capacitance of the transistor limits the maximum load impedance. For our experiment, we utilize a GS66504B GaN HEMT from GaN Systems, which has a nominal small-signal C_{oss} of 40 pF at 200 V drain-to-source. The maximum load impedance for our application is 24 Ω from

$$R_{L,\max} = \frac{1}{34.22 f_s C_{\text{oss}}}. \tag{28}$$

This means the n value for the transformers must be greater than 1.83 since the rectifier's input impedance is scaled by $1/n^2$ on the inverter side. Thus, we can utilize our experimental transformers for this converter. To obtain the proper power delivered to the load, we size C_s to achieve the target RLC load network impedance since L_s is fixed by the transformer. Fig. 28 shows an image of the inverter system. We used the same inverter and rectifier to drive all three different transformers. Table XVI lists the components for the experiment.

Fig. 29 displays the photograph of the converter, the drain and gate waveforms of the inverter side, and the rectifier diode waveforms. Lastly, Table XVII lists the performance efficiencies for the converters.

As shown in Fig. 29 by the drain waveforms of the converters, the active switches achieve ZVS with similar voltage stress across the three converters, thus eliminating switching loss.

TABLE XVI
BILL OF MATERIALS FOR THE INVERTER AND RECTIFIER IMPLEMENTED IN THIS EXPERIMENT

Component	Value
C_{in}	18.8 µF 100 V X7R, 50 nF 1kV C0G capacitors
L_f	700 nH 14 AWG wire-wound toroidal inductor
Q_1	GS66504B GaN Systems 650 V 100 mΩ GaN HEMT
C_p	N/A
C_s (nested)	540 pF 500 V C0G capacitor
C_s (stacked)	286 pF 500 V C0G capacitor
C_s (interleaved)	356 pF 500 V C0G capacitor
C_B	4.7 nF 2kV X7R capacitors
D_1, D_2	STPSC406B STMicroelectronics 600 V SiC Schottky Diode
C_{out}	0.1 µF 630 V X7R capacitor
R_L	400 Ω 400 W dc dummy load
Gate Drive	LM5114B Texas Instruments low-side gate driver

Because the voltage stress, power delivery, and components other than the rectifiers' input capacitance are similar across the converters, the power devices experience equivalent power losses, meaning the main contribution toward the difference in efficiencies is the transformers. As expected, the interleaved and stacked transformers achieve similar efficiencies due to having similar resistance matrix parameters. Both efficiencies are higher than the nested transformer efficiency which suffers

TABLE XVII
CONVERTER PARAMETERS FOR THE DIFFERENT TRANSFORMERS

	Nested	Stacked	Interleaved
Input voltage [V]	45	46.5	45
Input current [A]	2.91	2.67	2.73
Output voltage [V]	201	201	204
Output current [A]	0.5	0.5	0.51
Input power [W]	131	124	123
Output power [W]	101	101	104
Efficiency	77%	81%	85%

from significant losses from having a large secondary winding resistance.

VII. CONCLUSION

This article features multiple transformer designs suitable for HF/very-high-frequency (VHF) power conversion applications. The first is a nested toroidal structure, where the N^2 fluxes of the toroids are coupled. The second is a stacked structure, where the one-turn fluxes are linked, and the N^2 flux of each toroid determines and confines the leakage field. The third features a standard parallel-winding interleaved transformer. We include for all three transformer configurations design equations, simulation results from COMSOL Multiphysics, and physical examples including converter demonstrations switching at 30 MHz. There are various benefits and disadvantages when selecting between the three different transformers. For example, the interleaved transformer has the simplest fabrication procedure but is limited in inductance matrix parameters. The stacked transformer has full control over leakage inductance but couples the one-turn flux leading to poor field confinement. The nested transformer has excellent field confinement and a wide selection of the inductance matrix but suffers from proximity losses in the secondary. The interleaved transformer has good field confinement and lower losses but necessitates more effort to achieve the target inductance matrix, due to the lack of precise design equations for the mutual inductance. Regardless of the choice in transformer selection, 3-D printing offers viable opportunities in low-cost manufacturing of air-core magnetic components capable of high-frequency power transfer. These components offer much more design flexibility compared to commercial components and are more realistic to accurately model in FEM software, particularly with the publicly available design automation scripts provided.

ACKNOWLEDGMENT

The authors would like to thank J. Barker and Artcraft Plating & Finishing for providing the electroplating services of the transformer scaffolds. The authors would also like to thank Maker lab64 at Stanford for discussion and assistance in the 3-D printing procedure.

REFERENCES

[1] Z. Tong. 3-D printed inductors and transformer FEM modeling. (2019) [Online]. Available: https://github.com/zikangtong/SUPER-Lab-Magnetics
[2] Z. Tong, W. D. Braun, and J. M. Rivas-Davila, "3-D printed air-core toroidal transformer for high-frequency power conversion," in *Proc. 20th Workshop Control Model. Power Electron*, Jun. 2019, pp. 1–7.
[3] J. M. Rivas, D. Jackson, O. Leitermann, A. D. Sagneri, Y. Han, and D. J. Perreault, "Design considerations for very high frequency dc-dc converters," in *Proc. 37th IEEE Power Electron. Specialists Conf.*, Jun. 2006, pp. 1–11.
[4] R. C. N. Pilawa-Podgurski, A. D. Sagneri, J. M. Rivas, D. I. Anderson, and D. J. Perreault, "Very high frequency resonant boost converters," in *Proc. IEEE Power Electron. Specialists Conf.*, Jun. 2007, pp. 2718–2724.
[5] D. J. Perreault *et al.*, "Opportunities and challenges in very high frequency power conversion," in *Proc. 24th Annu. IEEE Appl. Power Electron. Conf. Expo.*, Feb. 2009, pp. 1–14.
[6] J. S. Glaser, J. Nasadoski, and R. Heinrich, "A 900 W, 300 V to 50 V dc-dc power converter with a 30 MHz switching frequency," in *Proc. 24th Annu. IEEE Appl. Power Electron. Conf. Expo.*, Feb. 2009, pp. 1121–1128.
[7] A. Sagneri, "Design of miniaturized radio-frequency dc-dc power converters," Ph.D. dissertation, Dept. Elect. Eng. Comput. Sci., Massachusetts Inst. of Tech., Cambridge, MA, USA, 2012.
[8] J. W. Kolar, J. Biela, S. Waffler, T. Friedli, and U. Badstuebner, "Performance trends and limitations of power electronic systems," in *Proc. 6th Int. Conf. Integr. Power Electron. Syst.*, Mar. 2010, pp. 1–20.
[9] C. P. Steinmetz, "On the law of hysteresis," *Trans. Amer. Inst. Elect. Eng.*, vol. IX, no. 1, pp. 1–64, Jan. 1892.
[10] J. Li, T. Abdallah, and C. R. Sullivan, "Improved calculation of core loss with nonsinusoidal waveforms," in *Proc. Conf. Rec. IEEE Ind. Appl. Conf.. 36th Annu. Meet.*, Sep. 2001, vol. 4, pp. 2203–2210.
[11] J. Muhlethaler, J. Biela, J. W. Kolar, and A. Ecklebe, "Improved core-loss calculation for magnetic components employed in power electronic systems," *IEEE Trans. Power Electron.*, vol. 27, no. 2, pp. 964–973, Feb. 2012.
[12] S. Barg, K. Ammous, H. Mejbri, and A. Ammous, "An improved empirical formulation for magnetic core losses estimation under nonsinusoidal induction," *IEEE Trans. Power Electron.*, vol. 32, no. 3, pp. 2146–2154, Mar. 2017.
[13] P. L. Dowell, "Effects of eddy currents in transformer windings," *Proc. Institution Elect. Eng.*, vol. 113, no. 8, pp. 1387–1394, Aug. 1966.
[14] W. G. Hurley, E. Gath, and J. G. Breslin, "Optimizing the ac resistance of multilayer transformer windings with arbitrary current waveforms," *IEEE Trans. Power Electron.*, vol. 15, no. 2, pp. 369–376, Mar. 2000.
[15] Xi Nan and C. R. Sullivan, "An improved calculation of proximity-effect loss in high-frequency windings of round conductors," in *Proc. IEEE 34th Annu. Conf. Power Electron. Specialist*, Jun. 2003, vol. 2, pp. 853–860.
[16] W. D. Braun, L. Gu, G. Scott, and J. Rivas-Davila, "MRI compatible dc modulator for an envelope tracking transmitter," in *Proc. 20th Workshop Control Model. Power Electron.*, Jun. 2019, pp. 1–4.
[17] Y. Han, G. Cheung, A. Li, C. R. Sullivan, and D. J. Perreault, "Evaluation of magnetic materials for very high frequency power applications," *IEEE Trans. Power Electron.*, vol. 27, no. 1, pp. 425–435, Jan. 2012.
[18] M. Seitz and M. Roeber, "Squeeze more performance out of toroidal inductors," *Power Electron. Technol.*, vol. 31, no. 8, pp. 30–33, 2005.
[19] M. Nigam and C. R. Sullivan, "Multi-layer folded high-frequency toroidal inductor windings," in *Proc. 23rd Annu. IEEE Appl. Power Electron. Conf. Expo.*, Feb. 2008, pp. 682–688.
[20] A. J. Yerman, W. A. Roshen, R. J. Charles, R. P. Alley, and K. D. T. Ngo, "Megahertz transformers for high density power conversion," *IEEE Trans. Compon., Hybrids, Manuf. Technol.*, vol. 14, no. 4, pp. 725–731, Dec. 1991.
[21] C. R. Sullivan, "Layered foil as an alternative to litz wire: Multiple methods for equal current sharing among layers," in *Proc. IEEE 15th Workshop Control Model. Power Electron.*, Jun. 2014, pp. 1–7.
[22] M. Chen, M. Araghchini, K. K. Afridi, J. H. Lang, C. R. Sullivan, and D. J. Perreault, "A systematic approach to modeling impedances and current distribution in planar magnetics," *IEEE Trans. Power Electron.*, vol. 31, no. 1, pp. 560–580, Jan. 2016.
[23] M. Etemadrezaei and S. M. Lukic, "Coated-strand litz wire for multi-megahertz frequency applications," *IEEE Trans. Magn.*, vol. 52, no. 8, pp. 1–11, Aug. 2016.

[24] A. J. Hanson, J. A. Belk, S. Lim, C. R. Sullivan, and D. J. Perreault, "Measurements and performance factor comparisons of magnetic materials at high frequency," *IEEE Trans. Power Electron.*, vol. 31, no. 11, pp. 7909–7925, Nov. 2016.
[25] C. R. Sullivan, J. Qiu, D. V. Harburg, and C. G. Levey, "Batch fabrication of radial anisotropy toroidal inductors," in *Proc. Int. Symp. 3D Power Electron. Integration Manuf.*, Jun. 2016, pp. 1–15.
[26] B. A. Reese, R. Joseph, and C. R. Sullivan, "Improved litz-wire designs for the MHz range," in *Proc. IEEE 19th Workshop Control Model. Power Electron.*, Jun. 2018, pp. 1–8.
[27] J. Schäfer, D. Bortis, and J. W. Kolar, "Optimal design of highly efficient and highly compact PCB winding inductors," in *Proc. IEEE 19th Workshop Control Model. Power Electron.*, Jun. 2018, pp. 1–8.
[28] M. K. Ranjram, P. Acosta, and D. J. Perreault, "Design considerations for planar magnetic terminations," in *Proc. IEEE 20th Workshop Control Model. Power Electron.*, Jun. 2019, pp. 1–8.
[29] A. L. F. Stein, P. A. Kyaw, and C. R. Sullivan, "Wireless power transfer utilizing a high-Q self-resonant structure," *IEEE Trans. Power Electron.*, vol. 34, no. 7, pp. 6722–6735, Jul. 2019.
[30] R. S. Yang, A. J. Hanson, B. A. Reese, C. R. Sullivan, and D. J. Perreault, "A low-loss inductor structure and design guidelines for high-frequency applications," *IEEE Trans. Power Electron.*, vol. 34, no. 10, pp. 9993–10005, Oct. 2019.
[31] C. R. Sullivan, W. Li, S. Prabhakaran, and S. Lu, "Design and fabrication of low-loss toroidal air-core inductors," in *Proc. IEEE Power Electron. Specialists Conf.*, Jun. 2007, pp. 1754–1759.
[32] S. Orlandi *et al.*, "Optimization of shielded PCB air-core toroids for high-efficiency dc-dc converters," *IEEE Trans. Power Electron.*, vol. 26, no. 7, pp. 1837–1846, Jul. 2011.
[33] J. Qiu, A. J. Hanson, and C. R. Sullivan, "Design of toroidal inductors with multiple parallel foil windings," in *Proc. IEEE 14th Workshop Control Model. Power Electron.*, Jun. 2013, pp. 1–6.
[34] H. Schneider, T. Andersen, A. Knott, and M. A. E. Andersen, "Optimizing dc-resistance of a foil wounded toroidal inductor combining MATLAB and COMSOL," in *Proc. Africon*, Sep. 2013, pp. 1–5.
[35] J. M. Lopez-Villegas, N. Vidal, and J. A. del Alamo, "Optimized toroidal inductors versus planar spiral inductors in multilayered technologies," *IEEE Trans. Microw. Theory Techn.*, vol. 65, no. 2, pp. 423–431, Feb. 2017.
[36] G. Zulauf, W. Liang, and J. Rivas-Davila, "A unified model for high-power, air-core toroidal PCB inductors," in *Proc. IEEE 18th Workshop Control Model. Power Electron.*, Jul. 2017, pp. 1–8.
[37] N. Lazarus, S. S. Bedair, and G. L. Smith, "Origami inductors: Rapid folding of 3-D coils on a laser cutter," *IEEE Electron. Device Lett.*, vol. 39, no. 7, pp. 1046–1049, Jul. 2018.
[38] S. Park, L. Gu, and J. Rivas-Davila, "60 V-to-35 kV input-parallel output-series dc-dc converter using multi-level class-DE rectifiers," in *Proc. IEEE Appl. Power Electron. Conf. Expo.*, Mar. 2018, pp. 2235–2241.
[39] S. C. Tang, S. Y. Hui, and H. S.-H. Chung, "Coreless printed circuit board (PCB) transformers with multiple secondary windings for complementary gate drive circuits," *IEEE Trans. Power Electron.*, vol. 14, no. 3, pp. 431–437, May 1999.
[40] W. Liang, L. Raymond, and J. Rivas, "3-D-printed air-core inductors for high-frequency power converters," *IEEE Trans. Power Electron.*, vol. 31, no. 1, pp. 52–64, Jan. 2016.
[41] W. Liang *et al.*, "Low-mass RF power inverter for cubesat applications using 3-D printed inductors," *IEEE J. Emerg. Sel. Topics Power Electron.*, vol. 5, no. 2, pp. 880–890, Jun. 2017.
[42] H. Schneider, T. Andersen, A. Knott, and M. A. E. Andersen, "Hybrid winding concept for toroids," in *Proc. IEEE Energy Convers. Congr. Expo. Asia Downunder*, Jun. 2013, pp. 936–940.
[43] S. Ramo, J. Whinnery, and T. V. Duzer, *Fields and Waves in Communication Electronics*, 3rd ed. Hoboken, NJ, USA: Wiley, 1994.
[44] W. G. Hurley, M. C. Duffy, J. Zhang, I. Lope, B. Kunz, and W. H. Wölfle, "A unified approach to the calculation of self- and mutual-inductance for coaxial coils in air," *IEEE Trans. Power Electron.*, vol. 30, no. 11, pp. 6155–6162, Nov. 2015.
[45] E. B. Rosa and F. W. Grover, *Formulas and Tables for the Calculation of Mutual and Self-Inductance*, 3rd ed. Washington: Govt. Print. Off., Dec. 1916.
[46] J. H. Spreen, "Electrical terminal representation of conductor loss in transformers," *IEEE Trans. Power Electron.*, vol. 5, no. 4, pp. 424–429, Oct. 1990.
[47] *Performing Impedance Analysis With the E5061B ENA Vector Network Analyzer*, Keysight Technologies, Santa Rosa, CA, USA, 2018.
[48] *700 B Series NP0 Porcelain and Ceramic Multilayer Capacitors*, American Technical Ceramics (ATC), Huntington Station, NY, USA, 2018.
[49] N. O. Sokal, "Class-E RF power amplifiers," *QEX*, vol. 204, no. 1, pp. 9–20, 2001.

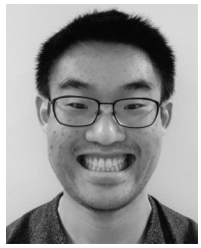

Zikang Tong (Student Member, IEEE) received the B.S. degree in electrical engineering with highest honors from the University of Illinois at Urbana-Champaign (UIUC), Champaign, IL, USA, in 2017, and the M.S. degree from Stanford University, Stanford, CA, USA, in 2019. He is currently working toward the Ph.D. degree in electrical engineering with Stanford University.

He is interested in building next-generation power electronic devices and components, including power semiconductors, passives, and magnetics, modeling, and applications for these technologies.

Weston D. Braun (Student Member, IEEE) received the B.S. and M.Eng. degrees in electrical engineering and computer science from the Massachusetts Institute of Technology, Cambridge, MA, USA, in 2017 and 2018, respectively. He is currently working toward the Ph.D. degree in electrical engineering with Stanford University, Stanford, CA, USA.

His current research interests include high-frequency switch-mode inverters and power conversion, computational power electronics optimization, and electronic design automation.

Juan Manuel Rivas-Davila (Senior Member, IEEE) was born in Mexico City, Mexico. He received the B.A.Sc. degree from the Monterrey Institute of Technology, Monterrey, Mexico, in 1998, and the S.M. and Sc.D. degrees from the Laboratory of Electromagnetic and Electronic Systems, Massachusetts Institute of Technology, Cambridge, MA, USA, in 2003 and 2006, respectively.

From 2007 to 2011, he was a Power Electronics Engineer with the High-Frequency Power Electronics Group at the General Electric Global Research Center, Niskayuna, NY, USA. From 2011 to 2013, he was an Assistant Professor with the University of Michigan, Ann Arbor, MI, USA. In 2014, he joined Stanford University, Stanford, CA, USA, as an Assistant Professor with the Electrical Engineering Department. His research interests include power electronics, RF power amplifiers, resonant converters, soft-switching topologies, and the design of air-core passive components for VHF power conversion.